Multibody System Dynamics
https://doi.org/10.1007/s11044-025-10095-9

RESEARCH

Study on bipedal running on compliant ground using hybrid zero dynamics controller

Yinnan Luo[1] · Philipp Arbogast[1] · Ulrich J. Römer[2] · Marten Zirkel[3] · Lena Zentner[3] · Alexander Fidlin[1]

Received: 5 November 2024 / Accepted: 23 July 2025

Abstract
We present a hybrid zero dynamics control design to develop stable, energy-efficient running gaits for a bipedal robot on compliant ground, extending previous work focused on rigid surfaces. The robot, modeled with five rigid segments and four actuated joints with point feet, has a running gait represented as a periodic hybrid dynamical system with two continuous phases and two discrete transitions. Non-slipping contact during single support is modeled using nonlinear viscoelastic contacts. Using virtual constraints, we represent the gait through reduced-order hybrid invariant zero dynamics. Periodic solutions are found via a multiple shooting method, and energy-efficient gaits are optimized by adjusting the reference trajectory within a sequential quadratic programming framework, incorporating stability and feasibility constraints. Orbital stability is assessed using Floquet theory. Ground compliance increases the dimension of the invariant zero dynamics manifold and introduces sensitivity in the contact phase equations. We overcome these challenges through a multiple shooting formulation and orthogonal projection of the monodromy matrix, isolating critical Floquet multipliers. This enables stable, efficient running gaits on compliant ground. Ground compliance does not inherently reduce energy efficiency and can enhance it despite additional contact dissipation. Moreover, compliant ground reduces impulsive landing forces, mitigating mechanical stress on the robot.

Keywords Bipedal robot · Bipedal running · Compliant ground · Hybrid zero dynamics control

1 Introduction

In recent years, the development of bipedal humanoid robots has accelerated, leading to diverse applications across various complex environments. The interaction between a robot's foot and the ground has garnered increasing research interest [1, 2]. Most robots feature numerous degrees of freedom, either passive [3] or actuated by electric or hydraulic drive trains, which follow different control strategies [4]. When modeling biped robots as dynamic multi-body systems, the interaction with the ground can be described either as a non-smooth, discontinuous mapping or as a continuous process with its own dynamics [5].

Specifically, the non-smooth contact approach is applicable when the ground is assumed to be perfectly rigid, a common assumption in many control designs where ground deformation is considered negligible compared to the robot's larger-scale movement [6]. In this case,

Extended author information available on the last page of the article

contact is modeled as an instantaneous impact, resulting in discontinuities in the system's state [7]. Studies such as [8] propose formulations for managing non-smooth impacts with friction, while hybrid dynamical systems incorporating both sticking and slipping behavior have been used to model biped locomotion in [9].

In bipedal robotics, compliance is typically introduced not through the ground but via deformable segments in robot platforms such as MABEL [10], Cassie [11], DURUS [12], ATRIAS [13], or the system described in [14], while the ground is still assumed to be rigid. The case of a robot with rigid segments interacting with a significantly deformable terrain is far less studied. In such cases, the non-instantaneous contact process is approximated by the continuous dynamics of the colliding objects [15]. The continuous deformation of the ground, determined by its reaction force-indentation characteristics, is crucial for modeling the robot's stance phase. Deciding on appropriate ground parameters is essential, as they often depend on the geometry and material properties of the colliding objects [16]. If the contact process is assumed to be quasi-static, the force-deformation relationship can be modeled using nonlinear spring models, such as those suggested by Hertz [17]. Additionally, damping is often considered in reaction force models to account for energy dissipation, according to [18]. Various viscoelastic models have been proposed in the literature for normal contact [19–22], and for coupled normal and tangential compliant contacts [23]. Studies such as [24] introduce simulation techniques to address friction at the contact point. Advanced finite element simulations also support the approximation of more detailed contact behaviors in data-driven approaches for complex surfaces [25], while other data-driven methods rely on experimental measurements [26].

Among various control paradigms [4], the inverted pendulum model represents a foundational methodology for the approximation of bipedal locomotion [27]. The zero-moment point (ZMP) control approach stands as one of the most prevalently employed strategies, specifically tailored for fully or over-actuated robotic systems equipped with multiple actuators to facilitate both walking [28, 29] and running [30]. The goal of ZMP control is to keep the zero-moment point within a support polygon [31]. More recently, the contact-wrench-sum control criteria alternatively consider the aggregated wrench that is generated by the contact and the gravitation being equal to the change of the robot's linear and rotational momentum with respect to the center of mass [32], enabling a broader range of contact scenarios to be evaluated [33]. Meanwhile, under-actuated robots have drawn considerable interest due to their high energy efficiency [34]. The Hybrid Zero Dynamics (HZD) controller has been successfully implemented for both planar walking [35] and running [36], as well as for 3D under-actuated robots [37].

Despite differences in control approaches, the ground surface is generally modeled as rigid and monolithic. However, extensions that include compliant ground behaviors can be found, for example in [38], which developed an optimization approach using human walking patterns, captured via cameras and force plates, to estimate optimal gaits for a planar robot model. The virtual model control concept, which uses virtual components (like springs and dampers) to simulate the interaction between the robot and the environment, enables the modeling of compliant ground [39]. The drawback of this approach is that selecting the appropriate virtual components requires a deep understanding of, and experience with, the specific robot system. Furthermore, another approach is studied in [40], which developed an HZD controller for RABBIT (a planar biped robot with five rigid body segments) on rigid ground and validated the controller's robustness by simulating the walking gait on compliant terrain. In [41], a time-based HZD controller was designed to generate bipedal walking gaits, incorporating either an instantaneous or non-instantaneous double support phase on compliant ground. To reduce the numerical complexity, this method first generates optimal gaits on rigid ground before applying them to compliant terrain.

Contrary to previous studies, this paper examines the adoption of the HZD framework for the generation of stable and energy-efficient running gaits on a compliant ground. The challenges associated with the stability analysis are of considerable interest, particularly due to the complexities of numerical handling under these conditions. Additionally, this study seeks to discern whether running on a compliant ground surface is less efficient than on a rigid one, owing to the contact's dissipative properties. Can the elasticity of the ground mitigate this inefficiency in certain scenarios?

A five-link robot model is utilized, as it offers the most elementary configuration necessary to facilitate the lift-off motion of the lower leg around the knee joint. A point foot is modeled at the stance leg's end, adhering to the Hertz theory, allowing us to describe indentation and damping dissipation in the normal direction with one penetration variable and its derivative. Implementing a sophisticated foot in contact dynamics augments the robot's degrees of freedom, requiring stress integration over a dynamic pressure field defined by the foot's geometry. Despite enhancing the controller's robustness and aligning more closely with human locomotion, this complexity complicates controller design and understanding the impact of ground deformation on movement. To achieve our research aim of validating simulation results with a robotic prototype through real experiments, employing a point foot model is fundamentally advantageous for system development. Our study thus commences with this basic model, allowing for advancement to more complex foot models in subsequent research.

The HZD control approach facilitates the generation of optimal gaits with high energy efficiency by utilizing the system's passive dynamics, particularly the free swinging of the robot's segments, to aid in locomotion. This controller is applied to an under-actuated biped, where there are fewer available actuators than degrees of freedom. The viscoelasticity of the ground causes rapid changes in velocity and acceleration during contact, resulting in a stiff numerical problem. This stiffness contrasts significantly with the dynamics during the flight phase of running, complicating the adaptation of the numerical integration step size, especially during phase transitions, when using a single shooting method [42].

To address this issue, the multiple shooting method [43] is employed, utilizing advanced ordinary differential equation (ODE) solvers. These solvers efficiently handle the stiff reduced-order zero dynamics during the compliant contact phase, while using larger adaptive integration step sizes for the flight phase dynamics. An alternative approach, the direct collocation method, as presented in [44], generates biped running gaits with multiple inelastic impacts by formulating the full-order system dynamics as optimization constraints using the Euler integration scheme. In particular, [45] introduces a novel scalable collocation method designed to manage high degrees of underactuation within the HZD framework.

However, further investigation is required to determine whether the collocation method is suitable for handling the stiff dynamics during the compliant contact phase in our case, where very small time steps are necessary in the discretization scheme. Additionally, minimizing trajectory drifts requires advanced techniques, such as those proposed in [46], which is crucial because even minor kinematic drifts can generate large (unphysical) response forces from the ground. Consequently, we opt for the multiple shooting approach to gain initial insights into how ground compliance affects the running gait.

The optimal reference running gait, postulated to be periodic and characterized by a constant average velocity, is established through an offline optimization process aimed at maximizing energy efficiency, designated as the objective function. The stability and physical feasibility of the running gait are ensured by means of inequality constraints within the optimization framework, which is addressed using the sequential quadratic programming (SQP) algorithm. While a plethora of optimization-based controllers, including optimal control [47] and model predictive control [48], have been devised for the purpose of tracking

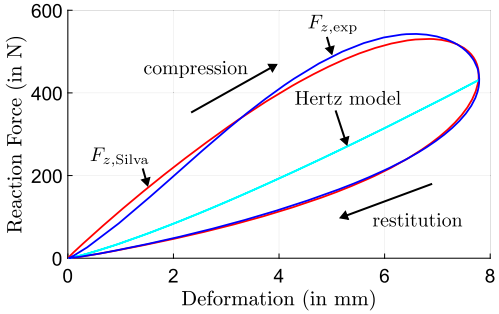

Fig. 1 Normal reaction force on the compliant ground determined using models $F_{z,\text{Silva}}$ from the equation (1b) (in red) and $F_{z,\text{exp}}$ from the equation (2) (in blue), which are compared to the static Hertz model (in light blue)

reference trajectories on real robot systems, the current study concentrates exclusively on the trajectory optimization for running on compliant ground. The outcomes are juxtaposed with those of running on rigid ground presented in existing literature, with respect to gait stability and energy efficiency.

The manuscript is structured as follows: Sect. 2 presents an overview of the modeling and simulation process; Sect. 3 introduces the robot model for running and the compliant ground model; Sect. 4 discusses the control design for running on compliant ground; Sect. 5 describes the optimization process for generating periodic, energy-efficient reference motion; Sect. 6 presents the optimization results, including efficiency and stability, and discusses the effect of ground compliance on the running gait; Sect. 7 concludes the study with a summary and outlook on future research.

2 Approach overview

This section provides an overview of the process for simulating and optimizing a biped robot's running gaits on compliant ground. The primary aim of this study is to explore how ground compliance affects the robot's locomotion, particularly with respect to energy efficiency and stability. The problem setup begins with a qualitative description of the compliant ground in Sect. 2.1. The bipedal running gaits are defined in Sect. 2.2, and are generated by the controller described in Sect. 2.3. In Sect. 2.4, an offline optimization process is employed to produce the optimal periodic reference motion, with an emphasis on maximizing energy efficiency.

2.1 Contact with compliant ground

The contact with deformable ground is modeled as a nonlinear viscoelastic element. For an initial understanding, Fig. 1 illustrates the reaction force in the normal direction as a function of deformation based on different models. The Hertz contact model disregards energy dissipation during contact, resulting in identical force-indentation curves for compression and restitution. In contrast, the models proposed in [49] and [22] account for energy dissipation through nonlinear damping, producing a hysteresis effect in the force diagram. In this study, we simplify the modeling of normal and tangential reaction forces by treating them in a decoupled manner, focusing only on stiction at the non-slipping stance foot [24, 50] (see Sect. 3.1 for further details). The proposed control design remains adaptable, allowing for the inclusion of more complex compliant contact models in future.

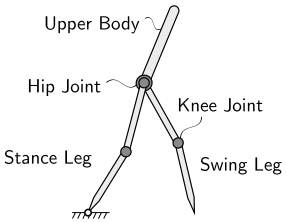

Fig. 2 The five-link robot model in contact with rigid ground via its stance leg

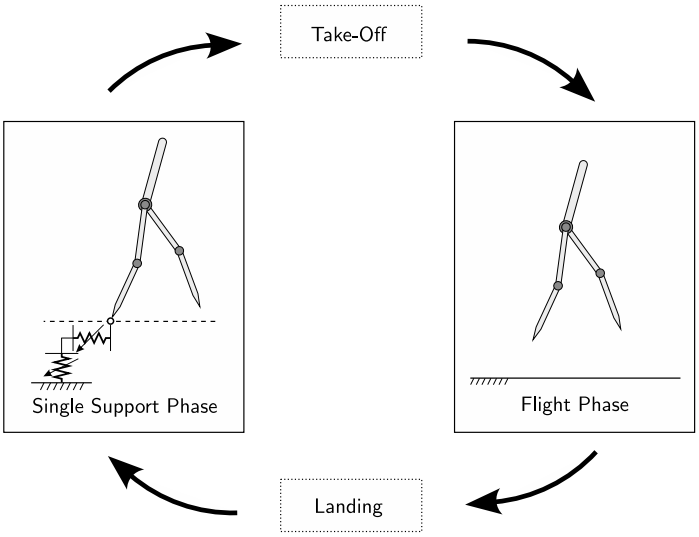

Fig. 3 Periodic running gait consisting of continuous single support and flight phases and discontinuous take-off and landing events

2.2 Periodic running gait

Our research utilizes a planar robot model (Fig. 2) comprising five rigid body segments, representing the upper body, two thighs, and two shanks. These segments are connected by four revolute joints at the hips and knees, which are actuated by electric motors. The lower end of each leg is modeled as a point foot, ensuring that no torque is transmitted around the stance foot between the robot body and the ground. This point foot design also aligns with the assumptions of the Hertz contact model, which is used to estimate the contact force.

At a constant average speed (step length over step duration), the running gait is assumed to be periodic. It consists of a repeating sequence: $\ldots \Rightarrow$ single support phase $\Rightarrow$ take-off $\Rightarrow$ flight phase $\Rightarrow$ landing $\Rightarrow \ldots$, as visualized in Fig. 3.

2.3 Controller design

We extend the hybrid zero dynamics controller as presented in [51] to accommodate the execution of running gaits on compliant ground. The primary distinction from traditional control on rigid surfaces lies in the incorporation of two additional degrees of freedom resulting from ground deformation, specifically in the normal and tangential directions. Figure 4 illustrates the configuration of the feedback controller during the single support phase.

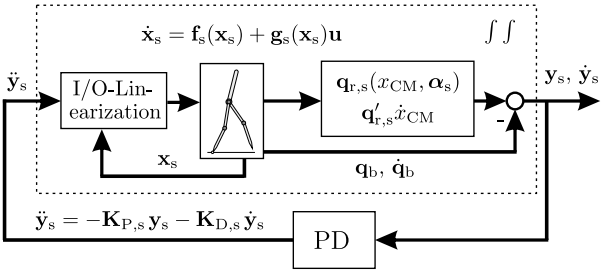

Fig. 4 Feedback control in the single support phase

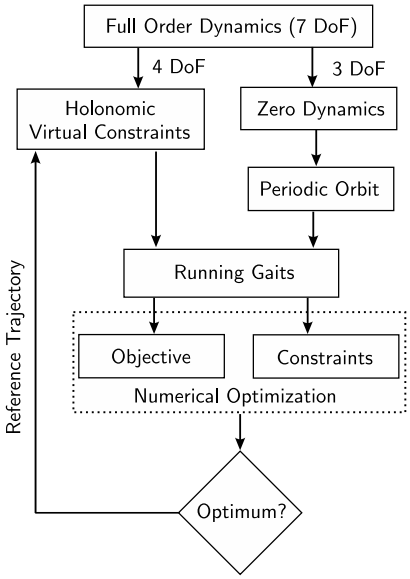

Fig. 5 Process of simulating and optimizing periodic gaits employing numerical optimization

This feedback mechanism is designed to align the actuated joints with their reference trajectories, thereby imposing the virtual constraints within these joints. Assuming the strict adherence to the virtual constraints, the periodic running gait of the full-order robot system is represented on the invariant zero dynamics manifold with a reduced order.

2.4 Gait generation by optimization

As illustrated in Fig. 5, the generation of efficient and stable running gaits is conceptualized as an offline optimization process focused on minimizing energy consumption during locomotion. The reference trajectories of the actuated joint angles act as the parameters to be optimized. Periodic solutions that describe the running gait are determined via a multiple shooting method, integrated into the optimization framework. The conditions of stability and feasibility for the resultant running gait are addressed as equality and inequality constraints within the optimization, which is resolved utilizing a SQP algorithm.

3 Model description

We investigate a planar robot model that consists of five rigid body segments representing the upper body, two thighs, and two shanks, connected by four revolute joints actuated by integrated electric drive trains. Various control concepts have been developed for this five-link robot, which has the simplest configuration that allows for foot lift-off due to the knee joint's degree of freedom. The primary contribution of the present research is extending this rigid body model to simulate running gaits on compliant ground. We assume minimal contact area between the lower end of the shank and the ground, modeling the foot as a point contact on a deformable surface. The stance foot without slipping on the ground is regarded as an ideal pivot without resistance.

The running gait is assumed to be periodic with a constant average speed, defined as the step length divided by the step duration. More specifically, the gait comprises four alternating phases: single support (SSP) and flight phases (FLP), governed by continuous dynamics, and the take-off and landing events, modeled as instantaneous, discontinuous mappings. During the SSP, the robot is supported by a single stance leg, while the swing leg moves forward without contacting the ground. SSP concludes with the take-off event, occurring when the normal reaction force at the stance foot becomes zero. The FLP follows, where the robot's center of mass follows a ballistic trajectory, as air resistance is neglected. The FLP ends with the landing event, marked by foot contact with the ground.

The organization of this section is as follows: Sect. 3.1 elucidates the compliant ground model; Sects. 3.2 and 3.3 present the continuous models for the FLP and SSP, respectively. Sections 3.4 and 3.5 discuss the discrete transition events of take-off and landing, respectively.

3.1 Compliant ground model

In the present study, we define the ground deformation $\boldsymbol{\delta} := [\delta_x, \delta_z]^\top$ and the time derivative $\dot{\boldsymbol{\delta}} := [\dot{\delta}_x, \dot{\delta}_z]^\top$ in the tangential $\vec{e}_x$ and the normal direction $\vec{e}_z$ of the ground surface, respectively. As specified in the SSP in Sect. 3.3, $\boldsymbol{\delta}$ and $\dot{\boldsymbol{\delta}}$ correspond to the position and velocity of the stance point foot, which can therefore be expressed as functions of $\mathbf{q}_\mathrm{f}$ and $\dot{\mathbf{q}}_\mathrm{f}$.

Among the various models, we started with the proposal of Silva et al. [49], which approximate both tangential and normal reaction forces of the compliant ground. In this study, different ground materials such as peat, clay, and sand are parameterized. In order to highlight the influence of the soft ground on the robot locomotion, we consider the softest material, namely peat. The contact force in $\vec{e}_x$- and $\vec{e}_z$-direction is modeled as

$$F_{x,\mathrm{Silva}} := K_x \delta_x(\mathbf{q}_\mathrm{f}) + \underbrace{\frac{\overline{B}_x}{\delta_{z,\max}}}_{B_x} \delta_z(\mathbf{q}_\mathrm{f}) \dot{\delta}_x(\mathbf{q}_\mathrm{f}, \dot{\mathbf{q}}_\mathrm{f}), \tag{1a}$$

$$F_{z,\mathrm{Silva}} := K_z \delta_z(\mathbf{q}_\mathrm{f}) + \underbrace{\frac{\overline{B}_z}{\left(\delta_{z,\max}\right)^{0.9}}}_{B_z} \left(\delta_z(\mathbf{q}_\mathrm{f})\right)^{0.9} \dot{\delta}_z(\mathbf{q}_\mathrm{f}, \dot{\mathbf{q}}_\mathrm{f}), \tag{1b}$$

with stiffness $K_x = 43{,}405\,\mathrm{Nm}^{-1}$ and $K_z = 56{,}840\,\mathrm{Nm}^{-1}$ and damping parameters $\overline{B}_x = 625\,\mathrm{Nsm}^{-1}$ and $\overline{B}_z = 715\,\mathrm{Nsm}^{-1}$. Note that the study in [49] estimates the parameters $\overline{B}_x$ and $\overline{B}_z$ for linear damping models, which are augmented by the maximum depth $\delta_{z,\max}$ of

the foot penetration into the ground to specify the nonlinear damping B_x and B_z. Given that this study aims to develop a general control strategy for generating bipedal running gaits on various compliant ground models, we treat the maximum value $\delta_{z,\max}$ in (1a)–(1b) as a nominal constant, which can be incorporated into the ground model's parameter uncertainty relative to real-world conditions. This assumption allows us to use a parameter-fitting procedure to identify ground parameters for other models that yield similar force-indentation characteristics to the materials studied in [49].

As noted in [22], one drawback of the expression in (1b) is that it can yield negative values, implying an adhesive reaction force. This contradicts the model's assumption of (dry) unilateral contact with the ground. These undesired adhesive forces often arise in scenarios involving forced contacts or when an object has multiple simultaneous contact points with the ground. This issue becomes particularly relevant when considering a non-instantaneous and continuous double support phase (DSP) for walking on compliant ground in future work, where both feet are expected to remain in contact with the ground. The robot model in the DSP is under-actuated because the ground's deformability means both stance feet lack constraints. Initial simulations of a non-instantaneous DSP demonstrate that imposing simultaneous contact at both stance feet complicates the numerical assessments due to stiff dynamics on compliant surfaces. Consequently, the optimization-based gait generation framework consistently aims to minimize the DSP duration to nearly zero.

For the robot model on rigid ground during the DSP, there is an over-actuation issue because the two stance legs form a closed kinematic chain, reducing the degrees of freedom to three—less than the four available actuators. A prior study [52] analyzed continuous DSP while walking on rigid terrain, demonstrating improved gait stability but decreased energy efficiency, due to the point foot model which does not allow for passive dynamics to enhance efficiency. Consequently, the increased computational complexity and decreased energy efficiency mean non-instantaneous DSP is excluded from this study. Instead, it is focused on running gaits similar to human running, involving contact only during the single support phase.

Nevertheless, although negative reaction forces can be prevented by imposing appropriate inequality constraints in the optimization process, it is beneficial to employ an alternative formulation that inherently avoids this problem. Therefore, the normal reaction force is determined by

$$F_{z,\exp} = K_{\exp} \exp\left(\eta \dot{\delta}_z(\mathbf{q}_\mathrm{f}, \dot{\mathbf{q}}_\mathrm{f})\right) \delta_z(\mathbf{q}_\mathrm{f})^\nu, \tag{2}$$

as proposed in [22]. The exponential function in (2) ensures that no negative (adhesive) normal forces occur. The parameters $K_{\exp}$, η, and ν are determined through a fitting process (see Fig. 6). This fitting aims to estimate the appropriate parameters in (2) to replicate similar deformation behaviors as in (1b), using ground parameters for peat from [49]. Specifically, we minimize the sum of squared errors between the contact velocity-deformation characteristics[1] produced by both models, starting from identical initial conditions.

Typically, the parameter ν depends on the geometry of the colliding objects. For example, $\nu = 3/2$ applies to a point model colliding with a deformable flat surface, according to Hertz's theory [17]. In this study, we also estimate ν by fitting it to existing data, yielding $\nu = 1.208$.

[1] An alternative approach could be to formulate the parameter fitting task to match the force-deformation diagram across different ground models, as shown in Fig. 1. However, since the primary focus of this study is the effect of compliant ground, we prioritize analyzing the evolution of the colliding objects' state variables, particularly positions and velocities.

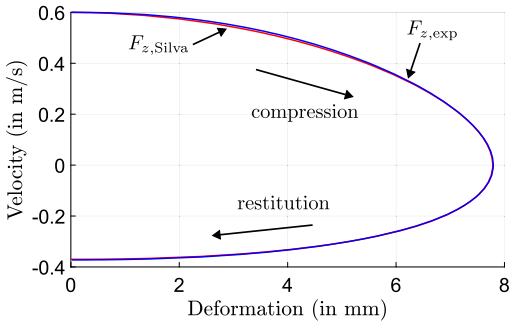

Fig. 6 Velocity of the contact foot over the ground deformation resulted from the normal force $F_{z,\text{Silva}}$ (red) and $F_{z,\text{exp}}$ (blue) with the fitted ground parameters

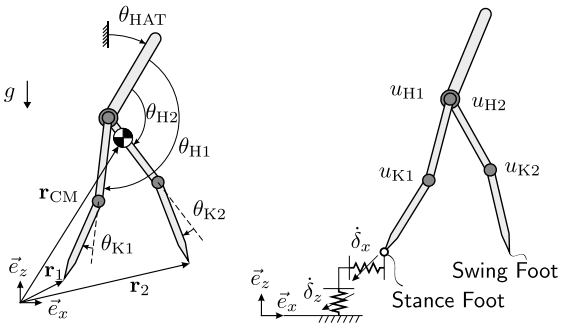

Fig. 7 Left: Five-link robot model in the flight phase. Right: Robot in the single support phase, with position $\mathbf{r}_1$ of the stance foot

As the tangential force can be either positive or negative, using the formulation in (2) to prevent negative forces is unnecessary. Thus, the force formulation $F_{x,\text{Silva}}$ in (1a), along with the suggested parameters, is adopted from the literature without modifications. The force model $F_{z,\text{exp}}$ according to (2) is used for the normal direction.

Identifying parameters in (2) is a drawback of utilizing the exponential function. Since stiffness and damping are closely linked, the parameter fitting via optimization might lead to non-uniqueness due to varying experimental data caused by minor measurement uncertainties. This non-uniqueness can result in significant differences in contact dynamics. Furthermore, the assumed decoupled normal and tangential forces complicate adjusting contact model parameters using a variable friction coefficient for specific conditions. Our primary aim is to extend the optimization framework to incorporate ground compliance within gaits generated by the HZD controller. Future research could explore similar contact force models using this framework.

3.2 Flight Phase (FLP) model

As shown in Fig. 7 (Left), the FLP model has seven DoF defined[2] by the coordinates $\mathbf{q}_\text{f} := [\mathbf{r}_\text{CM}^\top, \theta_\text{HAT}, \mathbf{q}_\text{b}^\top]^\top \in \mathcal{Q}_\text{f} \subset \mathbb{R}^2 \times \mathbb{T}^5$ and a five-dimensional torus $\mathbb{T}^5$. Here, $\mathbf{r}_\text{CM} := [x_\text{CM}, z_\text{CM}]^\top$ is the CoM position of the robot in the coordinate system $\{\vec{e}_x, \vec{e}_z\}$, θ_HAT is the upper body's absolute orientation, and $\mathbf{q}_\text{b} := [\theta_\text{H1}, \theta_\text{H2}, \theta_\text{K1}, \theta_\text{K2}]^\top$ are the angles of the four actuated joints with integrated electric drives producing the actuator torques $\mathbf{u} := [u_\text{H1}, u_\text{H2}, u_\text{K1}, u_\text{K2}]^\top$.

[2]Mathematical definitions are marked with :=.

Using Lagrange's equations as explained in [53, Sect. 3.5.1], the motion of the FLP is described by

$$\mathbf{M}_{\mathrm{f}}(\mathbf{q}_{\mathrm{f}})\,\ddot{\mathbf{q}}_{\mathrm{f}} + \boldsymbol{\Gamma}_{\mathrm{f}}(\mathbf{q}_{\mathrm{f}}, \dot{\mathbf{q}}_{\mathrm{f}}) = \mathbf{B}_{\mathrm{f}}\mathbf{u}. \tag{3}$$

$\mathbf{M}_{\mathrm{f}}$ is the mass matrix, $\boldsymbol{\Gamma}_{\mathrm{f}}$ represents the generalized forces including Coriolis and gravitational elements, and $\mathbf{B}_{\mathrm{f}} := [\mathbf{0}, \mathbf{I}_4]^\top$ is the actuation projection with a zero matrix and a 4×4 unit matrix. Considering the second-order nature of the system dynamics, the state space is constituted by the tangent bundle $T\mathcal{Q}_{\mathrm{f}}$ of the configuration space $\mathcal{Q}_{\mathrm{f}}$, as delineated in reference

$$T\mathcal{Q}_{\mathrm{f}} := \{\mathbf{x} := [\mathbf{q}_{\mathrm{f}}^\top, \dot{\mathbf{q}}_{\mathrm{f}}^\top]^\top \mid \mathbf{q}_{\mathrm{f}} \in \mathcal{Q}_{\mathrm{f}}, \dot{\mathbf{q}}_{\mathrm{f}} \in \mathbb{R}^7\}. \tag{4}$$

The vector field within $T\mathcal{Q}_{\mathrm{f}}$, as dictated by the equations of motion (3), is defined as

$$\dot{\mathbf{x}}_{\mathrm{f}} = \mathbf{f}_{\mathrm{f}}(\mathbf{x}_{\mathrm{f}}) + \mathbf{g}_{\mathrm{f}}(\mathbf{x}_{\mathrm{f}})\mathbf{u}, \qquad \mathbf{x}_{\mathrm{f}} \in T\mathcal{Q}_{\mathrm{f}}. \tag{5}$$

3.3 Single Support Phase (SSP) model

During the SSP (Fig. 7 (Right)), the stance leg contacts the ground with its point foot, generating reaction forces $\mathbf{F}_1 := [F_{1x}, F_{1z}]^\top$. The position $\mathbf{r}_1(\mathbf{q}_{\mathrm{f}}) := [x_1, z_1]^\top = \boldsymbol{\delta}$ (related to ground penetration) and the velocity vector $\dot{\mathbf{r}}_1(\mathbf{q}_{\mathrm{f}}, \dot{\mathbf{q}}_{\mathrm{f}}) := [\dot{x}_1, \dot{z}_1]^\top = \dot{\boldsymbol{\delta}}$ of the stance point foot can be expressed as functions of the coordinates $\mathbf{q}_{\mathrm{f}}$ and their time derivatives $\dot{\mathbf{q}}_{\mathrm{f}}$.

In accordance with the principle of virtual power, $\mathbf{F}_1$ and the Jacobian $\mathbf{J}_1 := (\partial\dot{\mathbf{r}}_1/\partial\dot{\mathbf{q}}_{\mathrm{f}})$ are present in the motion equation

$$\mathbf{M}_{\mathrm{f}}(\dot{\mathbf{q}}_{\mathrm{f}})\,\ddot{\mathbf{q}}_{\mathrm{f}} + \underbrace{\boldsymbol{\Gamma}_{\mathrm{f}} - \left(\frac{\partial\dot{\mathbf{r}}_1}{\partial\dot{\mathbf{q}}_{\mathrm{f}}}\right)^\top \mathbf{F}_1}_{\boldsymbol{\Gamma}_{\mathrm{gen,s}}(\mathbf{q}_{\mathrm{f}}, \dot{\mathbf{q}}_{\mathrm{f}})} = \mathbf{B}_{\mathrm{f}}\mathbf{u}, \tag{6}$$

where the three degrees of freedom—x_{CM}, z_{CM}, and θ_{HAT}—remain uncontrollable through actuation $\mathbf{u}$. Notably, the generalized force $\boldsymbol{\Gamma}_{\mathrm{gen,s}}$ is augmented by the reactive response of the compliant ground, which is formulated as a function dependent on the system states $(\mathbf{q}_{\mathrm{f}}, \dot{\mathbf{q}}_{\mathrm{f}})$, consistent with equation (3). Consequently, the vector field, as dictated by the equation of motion (6) during the SSP, is articulated in the state space $T\mathcal{Q}_{\mathrm{f}}$ as

$$\dot{\mathbf{x}}_{\mathrm{s}} = \mathbf{f}_{\mathrm{s}}(\mathbf{x}_{\mathrm{s}}) + \mathbf{g}_{\mathrm{s}}(\mathbf{x}_{\mathrm{s}})\mathbf{u}, \qquad \mathbf{x}_{\mathrm{s}} \in T\mathcal{Q}_{\mathrm{f}}. \tag{7}$$

3.4 Take Off (TO)

The TO is a discrete event transitioning state variables from the end of the SSP $(\mathbf{q}_{\mathrm{f,s}}^-, \dot{\mathbf{q}}_{\mathrm{f,s}}^-)$ to the start of the FLP $(\mathbf{q}_{\mathrm{f,f}}^+, \dot{\mathbf{q}}_{\mathrm{f,f}}^+)$, with smooth transitions in coordinates and velocities as shown in

$$\mathbf{q}_{\mathrm{f,s}}^- = \mathbf{q}_{\mathrm{f,f}}^+, \quad \dot{\mathbf{q}}_{\mathrm{f,s}}^- = \dot{\mathbf{q}}_{\mathrm{f,f}}^+. \tag{8}$$

The TO occurs on the surface $\mathbf{x}_{\mathrm{s}}^- := [(\mathbf{q}_{\mathrm{f,s}}^-)^\top, (\dot{\mathbf{q}}_{\mathrm{f,s}}^-)^\top]^\top \in \mathcal{S}_{\mathrm{s}}^{\mathrm{f}}$, when the normal reaction force $F_{1z}^- = 0$ at the stance foot $\mathbf{r}_1$ becomes zero.

3.5 Landing (LD) on compliant ground

The LD event on the surface $\mathcal{S}_{\mathrm{f}}^{\mathrm{s}}$ marks the culmination of the FLP as the anterior foot establishes contact with the ground, signified by the vertical displacement $z_2(\mathbf{q}_{\mathrm{f,f}}) = 0$ of the swing foot becoming null. Due to the compliance inherent in the massless ground model, transitions occur without impact, thereby ensuring a seamless transition where the terminal conditions $\mathbf{x}_{\mathrm{f}}^{-} := [(\mathbf{q}_{\mathrm{f,f}}^{-})^{\top}, (\dot{\mathbf{q}}_{\mathrm{f,f}}^{-})^{\top}]^{\top} \in \mathcal{S}_{\mathrm{f}}^{\mathrm{s}}$ of the FLP are directly mapped onto the initial conditions $\mathbf{x}_{\mathrm{s}}^{+} := [(\mathbf{q}_{\mathrm{f,s}}^{+})^{\top}, (\dot{\mathbf{q}}_{\mathrm{f,s}}^{+})^{\top}]^{\top}$ of the successive SSP. Furthermore, considering that the simulation of a singular step cycle is adequate for the representation of periodic motion, the roles of the leading and trailing limbs are interchanged during the landing phase:

$$\mathbf{q}_{\mathrm{f,s}}^{+} = \mathbf{R}_{-}^{+}\mathbf{q}_{\mathrm{f,f}}^{-}, \quad \dot{\mathbf{q}}_{\mathrm{f,s}}^{+} = \mathbf{R}_{-}^{+}\dot{\mathbf{q}}_{\mathrm{f,f}}^{-}. \tag{9}$$

It is important to observe that the CoM position undergoes a shift equivalent to exactly one step length $\mathbf{r}_{\mathrm{step}} := r_{\mathrm{step},x}\vec{e}_x + r_{\mathrm{step},z}\vec{e}_z$ following a complete step cycle. In order to reset the CoM position to its initial state, this displacement must be deducted from the final position ($\mathbf{r}_{\mathrm{CM}}^{+} = \mathbf{r}_{\mathrm{CM}}^{-} - \mathbf{r}_{\mathrm{step}}$). The subsequent states of the system are modified in accordance with the relabeling matrix

$$\mathbf{R}_{-}^{+} := \begin{bmatrix} \mathbf{I}_3 & \mathbf{0} \\ \mathbf{0} & \mathbf{R} \end{bmatrix}, \text{ with } \quad \mathbf{R} := \begin{bmatrix} 0 & 1 & 0 & 0 \\ 1 & 0 & 0 & 0 \\ 0 & 0 & 0 & 1 \\ 0 & 0 & 1 & 0 \end{bmatrix}. \tag{10}$$

4 Hybrid zero dynamics control

This section addresses the design of control strategies aimed at facilitating efficient running gaits on compliant terrains by employing extensions of the established HZD control framework as reported in the literature [53]. Specifically, the control strategy that incorporates virtual constraints during the FLP is derived from [53, Sect. 9.3.2]. In the reference, the ground surface is considered rigid, resulting in a two-dimensional zero dynamics manifold during the SSP. The current research effort is focused on enhancing the controller to incorporate compliant contact during the SSP, thereby yielding a six-dimensional zero dynamics manifold. To address the augmented dimensionality, we employ Floquet theory to evaluate the stability of the periodic solutions emerging from the hybrid zero dynamics.

The structure of this section is outlined as follows: Sect. 4.1 delineates the zero dynamics pertinent to the single support and flight phases. Section 4.2 develops a hybrid zero dynamics model that characterizes running gait. Section 4.3 elucidates the methodology for evaluating the stability of periodic running gaits.

4.1 Virtual constraints

The framework of virtual constraints is thoroughly explicated in [53, Sect. 5.1.2]. Fundamentally, feedback controllers are devised to nullify the output $\mathbf{y}_{\mathrm{s}}$ in the SSP, and $\mathbf{y}_{\mathrm{f}}$ in the FLP, defined as

$$\mathbf{y}_{\mathrm{s}} = \mathbf{h}_{\mathrm{s}}(\mathbf{x}_{\mathrm{s}}) = \mathbf{q}_{\mathrm{b}} - \mathbf{q}_{\mathrm{r,s}}(x_{\mathrm{CM}}, \boldsymbol{\alpha}_{\mathrm{s}}), \tag{11a}$$

$$\mathbf{y}_{\mathrm{f}} = \mathbf{h}_{\mathrm{f}}(\mathbf{x}_{\mathrm{f}}) = \mathbf{q}_{\mathrm{b}} - \mathbf{q}_{\mathrm{r,f}}(x_{\mathrm{CM}}, \boldsymbol{\alpha}_{\mathrm{f}}), \tag{11b}$$

wherein $\mathbf{q}_{\mathrm{r,s}} : \mathbb{R} \times \mathbb{R}^{4\times 7} \to \mathbb{R}^4$ and $\mathbf{q}_{\mathrm{r,f}} : \mathbb{R} \times \mathbb{R}^{4\times 7} \to \mathbb{R}^4$ function as the reference trajectory in the SSP and FLP, respectively. This trajectory is characterized by Bézier polynomials of sixth degree, encompassing parameters $\boldsymbol{\alpha}_{\mathrm{s}} \in \mathbb{R}^{4\times 7}$ and $\boldsymbol{\alpha}_{\mathrm{f}} \in \mathbb{R}^{4\times 7}$, as detailed in [53, Sect. 6.2]. The phase-dependent control strategy is implemented by choosing the horizontal position x_{CM} of the CoM as the independent variable, owing to its consistently monotonous increase throughout both the SSP and FLP.

The formulation elucidated in (11b) originates from the framework as outlined in [53, Sect. 9.3.2], wherein the feedback linearization approach as per [54] is employed to nullify the control output. Consequently, by utilizing the same methodological approach and presuming the complete fulfillment of virtual constraints absent of control inaccuracies, the zero dynamics manifolds within the SSP and FLP emerge as articulated in

$$\mathcal{Z}_{\mathrm{s}} := \{\mathbf{x}_{\mathrm{s}} \in T\mathcal{Q}_{\mathrm{f}} \,\|\, \mathbf{h}_{\mathrm{s}}(\mathbf{x}_{\mathrm{s}}) = \mathbf{0},\, \mathcal{L}_{\mathbf{f}_{\mathrm{s}}}\mathbf{h}_{\mathrm{s}}(\mathbf{x}_{\mathrm{s}}) = \mathbf{0}\}, \tag{12a}$$

$$\mathcal{Z}_{\mathrm{f}} := \{\mathbf{x}_{\mathrm{f}} \in T\mathcal{Q}_{\mathrm{f}} \,\|\, \mathbf{h}_{\mathrm{f}}(\mathbf{x}_{\mathrm{f}}) = \mathbf{0},\, \mathcal{L}_{\mathbf{f}_{\mathrm{f}}}\mathbf{h}_{\mathrm{f}}(\mathbf{x}_{\mathrm{f}}) = \mathbf{0}\}, \tag{12b}$$

encompassing both as smooth, six-dimensional invariant submanifolds embedded within $T\mathcal{Q}_{\mathrm{f}}$. Within this context, $\mathcal{L}_{\mathbf{f}_{\mathrm{s}}}$ and $\mathcal{L}_{\mathbf{f}_{\mathrm{f}}}$ denote the Lie derivative along the vector fields (7) of the SSP and (5) of the FLP, respectively.

Within the SSP zero dynamics manifold as referenced in $\mathcal{Z}_{\mathrm{s}}$, local coordinates $\mathbf{z}_{\mathrm{s}} := [\mathbf{q}_{\mathrm{z,s}}^{\top}, \mathbf{p}_{\mathrm{z,s}}^{\top}]^{\top}$, wherein $\mathbf{q}_{\mathrm{z,s}} := [\mathbf{r}_{\mathrm{CM}}^{\top}, \theta_{\mathrm{HAT}}]^{\top}$ and $\mathbf{p}_{\mathrm{z,s}} := \begin{bmatrix}\mathbf{I}_3 & \mathbf{0}\end{bmatrix}\mathbf{M}_{\mathrm{f}}(\mathbf{q}_{\mathrm{f}})\dot{\mathbf{q}}_{\mathrm{f}}$ serve as conjugates to $\mathbf{q}_{\mathrm{z,s}}$, are employed to delineate the zero dynamics as indicated in $\dot{\mathbf{z}}_{\mathrm{s}} = \mathbf{f}_{\mathrm{s,zero}}(\mathbf{z}_{\mathrm{s}})$, specifically articulated in

$$\dot{\mathbf{q}}_{\mathrm{z,s}} = \boldsymbol{\kappa}_{\mathrm{s},1}\left(\mathbf{q}_{\mathrm{z,s}}\right)\mathbf{p}_{\mathrm{z,s}}, \tag{13a}$$

$$\dot{\mathbf{p}}_{\mathrm{z,s}} = \boldsymbol{\kappa}_{\mathrm{s},2}\left(\mathbf{q}_{\mathrm{z,s}}, \mathbf{p}_{\mathrm{z,s}}\right), \tag{13b}$$

The components $\boldsymbol{\kappa}_{\mathrm{s},1}$ and $\boldsymbol{\kappa}_{\mathrm{s},2}$ are obtained by following the methodology delineated in [53, Equation (5.48)]. Due to the ground's compliance, equation (13a)–(13b) constitutes a stiff ordinary differential equation system.

Within the FLP zero dynamics manifold $\mathcal{Z}_{\mathrm{f}}$, the coordinates $\mathbf{z}_{\mathrm{f}} := [\mathbf{q}_{\mathrm{z,f}}^{\top}, \mathbf{p}_{\mathrm{z,f}}^{\top}]^{\top}$ include $\mathbf{q}_{\mathrm{z,f}} := [\mathbf{r}_{\mathrm{CM}}^{\top}, \theta_{\mathrm{HAT}}]^{\top}$ and $\mathbf{p}_{\mathrm{z,f}} := [\dot{\mathbf{r}}_{\mathrm{CM}}^{\top}, \sigma_{\mathrm{CM}}]^{\top}$, together with the generalized momentum $\sigma_{\mathrm{CM}} := \begin{bmatrix}\mathbf{0} & 1 & \mathbf{0}\end{bmatrix}\mathbf{M}_{\mathrm{f}}(\mathbf{q}_{\mathrm{f}})\dot{\mathbf{q}}_{\mathrm{f}}$ relative to the CoM. The zero dynamics are defined by equation $\dot{\mathbf{z}}_{\mathrm{f}} = \mathbf{f}_{\mathrm{f,zero}}(\mathbf{z}_{\mathrm{f}})$, as derived from reference [53, Equation (9.18)].

4.2 Hybrid zero dynamics

The running gait, characterized by an alternating sequence of $\ldots \Rightarrow$ single support phase, $\Rightarrow$ take-off, $\Rightarrow$ flight phase, $\Rightarrow$ landing $\Rightarrow \ldots$, is considered periodic at a given constant average speed $v_{\mathrm{avg}} := \ell_{\mathrm{step}}/t_{\mathrm{step}}$. Here, ℓ_{step} represents the step length and t_{step} denotes the step duration. The gait is structured upon the zero dynamics manifold, as delineated in (12a)–(12b), referred to as hybrid zero dynamics, and elaborated in

$$\Sigma_{\mathrm{ZD}} : \begin{cases} \dot{\mathbf{z}}_{\mathrm{s}} = \mathbf{f}_{\mathrm{s,zero}}(\mathbf{z}_{\mathrm{s}}), & \mathbf{z}_{\mathrm{s}} \notin \mathcal{S}_{\mathrm{s}}^{\mathrm{f}} \cap \mathcal{Z}_{\mathrm{s}}, \\ \mathbf{z}_{\mathrm{f}}^{+} = \boldsymbol{\Delta}_{\mathrm{s,zero}}^{\mathrm{f}}(\mathbf{z}_{\mathrm{s}}^{-}), & \mathbf{z}_{\mathrm{s}}^{-} \in \mathcal{S}_{\mathrm{s}}^{\mathrm{f}} \cap \mathcal{Z}_{\mathrm{s}}, \\ \dot{\mathbf{z}}_{\mathrm{f}} = \mathbf{f}_{\mathrm{f,zero}}(\mathbf{z}_{\mathrm{f}}), & \mathbf{z}_{\mathrm{f}} \notin \mathcal{S}_{\mathrm{f}}^{\mathrm{s}} \cap \mathcal{Z}_{\mathrm{f}}, \\ \mathbf{z}_{\mathrm{s}}^{+} = \boldsymbol{\Delta}_{\mathrm{f,zero}}^{\mathrm{s}}(\mathbf{z}_{\mathrm{f}}^{-}), & \mathbf{z}_{\mathrm{f}}^{-} \in \mathcal{S}_{\mathrm{f}}^{\mathrm{s}} \cap \mathcal{Z}_{\mathrm{f}}. \end{cases} \tag{14}$$

Within this framework, the discontinuous mappings $\mathbf{z}_{\mathrm{f}}^{+} = \boldsymbol{\Delta}_{\mathrm{s,zero}}^{\mathrm{f}}(\mathbf{z}_{\mathrm{s}}^{-})$ and $\mathbf{z}_{\mathrm{s}}^{+} = \boldsymbol{\Delta}_{\mathrm{f,zero}}^{\mathrm{s}}(\mathbf{z}_{\mathrm{f}}^{-})$ are determined via the evaluation of take-off, as articulated in (8), and landing, as detailed

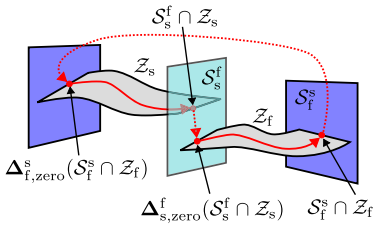

Fig. 8 Periodic solution of the continuous dynamics (solid red lines) and the discrete mappings (dashed red lines) of the hybrid zero dynamics of running

in (9), with regard to the zero dynamics manifolds $\mathcal{Z}_{\mathrm{s}}$ and $\mathcal{Z}_{\mathrm{f}}$ as specified in (12a)–(12b). A solution curve maintains invariance with respect to the discontinuous mappings provided the conditions $\boldsymbol{\Delta}_{\mathrm{s,zero}}^{\mathrm{f}}(\mathcal{S}_{\mathrm{s}}^{\mathrm{f}} \cap \mathcal{Z}_{\mathrm{s}}) \in \mathcal{Z}_{\mathrm{f}}$ and $\boldsymbol{\Delta}_{\mathrm{f,zero}}^{\mathrm{s}}(\mathcal{S}_{\mathrm{f}}^{\mathrm{s}} \cap \mathcal{Z}_{\mathrm{f}}) \in \mathcal{Z}_{\mathrm{s}}$, as illustrated in Fig. 8, are satisfied.

4.3 Stability of periodic reference solution

In this section, we examine the orbital stability of the non-smooth hybrid zero dynamics delineated in (14), which encapsulate periodic running gaits of the complete robot system, assuming strict adherence to the virtual constraints (11a)–(11b). Importantly, the zero dynamics are structured to remain invariant under the closed-loop system dynamics. For stable periodic orbits, referred to as limit cycles, minor perturbations or initial deviations from the running gait will diminish asymptotically, thereby enabling the disturbed motion to revert to the periodic reference gait at the desired constant velocity. Accordingly, the optimization framework is structured to confine the search space to stable limit cycles of the hybrid zero dynamics.

Various methods have been used to analyze the stability of periodic solutions in non-smooth dynamical systems, such as calculating the maximum Lyapunov exponents, as described in [55]. However, obtaining an accurate estimation of the Lyapunov exponents requires long numerical integration and careful orthonormalization to stabilize the evaluation, making this method impractical for our optimization framework. An alternative approach is to compute the Jacobian of the Poincaré map, as applied in the literature for running on rigid ground [51]. In our study, due to the high dimensionality of the zero dynamics, the Jacobian of the Poincaré map can only be approximated using automatic differentiation. However, given the computational inefficiency of this approach, we use the Poincaré map method solely to validate stability results determined by Floquet theory, which is introduced in this section.

Initially, in Sect. 4.3.1, we determine the monodromy matrix of the periodic solution in accordance with Floquet theory. Subsequently, in Sect. 4.3.2, we proceed to ascertain its eigenvalues, known as Floquet multipliers.

4.3.1 Monodromy matrix

Following the optimization process, the periodic solutions of the hybrid zero dynamics referenced in (14) are constructed utilizing the solution curve $\boldsymbol{\Phi}_{\mathrm{s}}\left(\mathbf{z}_{\mathrm{s}}^{+}, t\right)$ in the SSP and $\boldsymbol{\Phi}_{\mathrm{f}}\left(\mathbf{z}_{\mathrm{f}}^{+}, t\right)$ in the FLP, with $\mathbf{z}_{\mathrm{s}}^{+}$ and $\mathbf{z}_{\mathrm{f}}^{+}$ serving as the respective initial conditions. Furthermore, the total duration of a step $t_{\mathrm{step}} = t_{\mathrm{s}} + t_{\mathrm{f}}$ is characterized by the summation of t_{s} within the SSP and t_{f} within the FLP.

Subsequently, the methodology delineated in [56] is employed to determine the monodromy matrix of the hybrid dynamics, denoted as

$$\mathbf{M}_{\mathrm{Run}}\left(\mathbf{z}_{\mathrm{f}}^{-}, t_{\mathrm{step}}\right)=\frac{\partial \boldsymbol{\Phi}_{\mathrm{f}}\left(\mathbf{z}_{\mathrm{f}}^{+}, t_{\mathrm{f}}\right)}{\partial \mathbf{z}_{\mathrm{f}}^{+}} \mathbf{C}_{\mathrm{TO}}\left(\mathbf{z}_{\mathrm{s}}^{-}\right) \frac{\partial \boldsymbol{\Phi}_{\mathrm{s}}\left(\mathbf{z}_{\mathrm{s}}^{+}, t_{\mathrm{s}}\right)}{\partial \mathbf{z}_{\mathrm{s}}^{+}} \mathbf{C}_{\mathrm{LD}}\left(\mathbf{z}_{\mathrm{f}}^{-}\right). \tag{15}$$

Specifically, $\partial \boldsymbol{\Phi}_{\mathrm{f}}\left(\mathbf{z}_{\mathrm{f}}^{+}, t_{\mathrm{f}}\right) / \partial \mathbf{z}_{\mathrm{f}}^{+}$ and $\partial \boldsymbol{\Phi}_{\mathrm{s}}\left(\mathbf{z}_{\mathrm{s}}^{+}, t_{\mathrm{s}}\right) / \partial \mathbf{z}_{\mathrm{s}}^{+}$ represent the fundamental matrix solutions in the SSP and FLP, respectively, as derived according to reference [57, Sect. 3.2]. The derivatives of the discrete transitions, identified as saltation matrices $\mathbf{C}_{\mathrm{LD}}\left(\mathbf{z}_{\mathrm{f}}^{-}\right)$ and $\mathbf{C}_{\mathrm{TO}}\left(\mathbf{z}_{\mathrm{s}}^{-}\right)$, are obtained in compliance with reference [58, Equation (2)].

As illustrated in Fig. 8, the hyperplane utilized for the assessment of the monodromy matrix corresponding to the periodic solution is established on the landing surface $\mathbf{z}_{\mathrm{f}}^{-} \in \mathcal{S}_{\mathrm{f}}^{\mathrm{s}} \cap \mathcal{Z}_{\mathrm{f}}$. Given that the Floquet multiplier resulting from the analysis is insensitive to the selection of a hyperplane, situating this surface within the FLP effectively reduces numerical sensitivities. This effect is attributed to the lower stiffness of the equations governing the FLP zero dynamics compared to those in the SSP, a consequence of the compliance of the ground.

4.3.2 Floquet multiplier

According to the Floquet theory in [57, Sect. 3.2], the Floquet multipliers are the eigenvalues of the (6×6)-dimensional monodromy matrix $\mathbf{M}_{\mathrm{Run}}$, which describes how initial perturbations to a system state evolve along the periodic orbit over one period. Due to the autonomous nature of the system, there is always a trivial Floquet multiplier $\Lambda_0 = 1$, corresponding to perturbations along the flow direction. This multiplier merely causes a phase shift in the trajectory and does not impact orbital stability. The remaining five multipliers, particularly the one with the largest magnitude $|\Lambda|$, indicate the stability of the periodic orbit. Specifically, the periodic solution of the hybrid zero dynamics is stable if and only if the largest magnitude $|\Lambda| < 1$.

To facilitate the analysis of stability, the influence of the trivial Floquet multiplier $\Lambda_0 = 1$ is addressed by projecting the monodromy matrix $\mathbf{M}_{\mathrm{Run}}$ onto the nullspace of the tangent vector $\mathbf{f}_{\mathrm{f,zero}}\left(\mathbf{z}_{\mathrm{f}}^{-}\right)$ of the solution curve $\boldsymbol{\Phi}_{\mathrm{f}}\left(\mathbf{z}_{\mathrm{f}}^{+}, t\right)$ at the point of evaluation $\mathbf{z}_{\mathrm{f}}^{-}$, as this tangent vector $\mathbf{f}_{\mathrm{f,zero}}\left(\mathbf{z}_{\mathrm{f}}^{-}\right)$ serves as the associated eigenvector to the trivial multiplier Λ_0. In particular, five orthonormal basis vectors that span the orthogonal complement of $\mathbf{f}_{\mathrm{f,zero}}\left(\mathbf{z}_{\mathrm{f}}^{-}\right)$ are constructed[3] and organized into columns of a (6×5)-dimensional matrix $\mathbf{Q}_{\perp}$. The orthogonal projection described by

$$\mathbf{D}_{\Sigma,\mathrm{Run}} = \mathbf{Q}_{\perp}^{\top} \mathbf{M}_{\mathrm{Run}} \mathbf{Q}_{\perp}, \tag{16}$$

yields a reduced monodromy matrix $\mathbf{D}_{\Sigma,\mathrm{Run}} \in \mathbb{R}^{5\times5}$ that encompasses five eigenvalues[4] indicative of the non-trivial Floquet multipliers, which determine the orbital stability of the limit cycle. Specifically, the periodic solution is deemed stable if the largest eigenvalue magnitude $|\Lambda| < 1$ is less than one.

[3] As described in [59, Chap. 5], techniques such as Givens rotations and the Gram–Schmidt process are available for the construction of orthonormal basis vectors.

[4] The eigenvalues are computed numerically employing an iterative QR algorithm, as detailed in [59, Sect. 7.5].

5 Optimization of reference running gaits

A numerical optimization methodology is employed to determine physically feasible and periodic running gaits as generated by the controller described in Sect. 4. It is presumed that the virtual constraints in (11a)–(11b) are strictly adhered to, allowing the running gait to be characterized by the hybrid invariant zero dynamics with a reduced order. The reference trajectories for the actuated joint angles are parameterized using Bézier polynomials, as specified in [53, Sect. 6.2], which serve as the optimization parameters. The enhancement of energy efficiency in locomotion is the principal optimization objective, as discussed in Sect. 5.1. Assurance of physical feasibility and gait stability is accomplished through the imposition of equality and inequality constraints, as demonstrated in Sect. 5.2.

5.1 Optimization objective and parameters

The primary goal of the optimization is to generate stable running gaits on compliant ground with high energy efficiency. The efficiency is evaluated by the dimensionless cost of transport (CoT), defined as the optimization objective function:

$$f(\boldsymbol{x}_{\text{opt}}) = \text{CoT} := \frac{\sum_{i=1}^{4} \int_0^{t_{\text{step}}} \max\left(0,\ P_{\text{mech},i}\right) \mathrm{d}t}{mg\ell_{\text{step}}}, \tag{17}$$

where mg is the total weight, ℓ_{step} is the step length in one step period, and t_{step} is the step duration. The mechanical power $P_{\text{mech},i} = u_i \dot{q}_{\text{b},i}$, $i \in [1, 4]$ results from torque u_i of the motor and the joint's angular velocity $\dot{q}_{\text{b},i}$. Since no electric energy is recovered during deceleration, negative mechanical power (representing motor operation in generator mode) is excluded via the $\max(\cdot)$ operator. Additionally, Ohmic losses are neglected in this preliminary analysis, assuming $I^2 R \ll P_{\text{mech},i}$, $i \in [1, 4]$.

The running gait parameter set includes Bézier parameters, initial conditions, and step duration of the SSP and FLP, respectively:

$$\boldsymbol{x}_{\text{opt}} := \left[(\boldsymbol{\alpha}_{\text{s}})^{\top}, (\boldsymbol{\alpha}_{\text{f}})^{\top}, (\mathbf{z}_{\text{s}}^{+})^{\top}, (\mathbf{z}_{\text{f}}^{+})^{\top}, t_{\text{s}}, t_{\text{f}} \right]^{\top}. \tag{18}$$

5.2 Optimization constraints

The process of generating periodic solutions through multiple shooting is incorporated into the offline optimization procedure using the equality constraints described in Sect. 5.2.1. Feasibility of the running gaits is ensured by a set of physical conditions enforced through inequality constraints, as detailed in Sect. 5.2.2.

5.2.1 Periodic solution via multiple shooting

The periodic orbits of the hybrid zero dynamics for running consist of two continuous phases and two discrete mappings, as depicted in Fig. 8. Numerically integrating these solutions over extended evaluation periods, which involve transitions due to the discrete mappings, can be highly sensitive to small deviations in initial conditions or reference parameters. For instance, [42] highlights stability issues that arise when using adaptive time-step integration algorithms to detect contact events, a challenge when simulating running gaits. Specifically, during the flight phase, the integration step size is typically larger than in the single support phase due to the stiff system characteristics. If an inappropriate (i.e., overly large) step size

is used to detect contact events, it can result in significant, nonphysical ground penetration at the start of the single support phase, leading to abnormally large reaction forces and often causing the integration process to fail, particularly in single shooting methods.

In response to these numerical challenges, we adopt a multiple shooting method as described in [43]. This technique partitions the entire periodic solution into distinct continuous phases, with discrete transition events (such as contact detection) being treated as boundary conditions between phases, each governed by varying system dynamics. A prevalent method for enforcing these boundary conditions involves employing a root-finding algorithm such as Newton's method. Nevertheless, rather than utilizing this conventional approach, we integrate the equality constraints directly into the optimization process to enforce boundary conditions within the multiple shooting method. In particular, the stiff differential equations associated with the SSP are addressed utilizing the "RadauIIA5" solver, while the non-stiff equations involved in the FLP are resolved via the efficient "Tsit5" solver. These solvers are sourced from the Julia package *DifferentialEquations.jl*. The transitional events, namely take-off as delineated in (8) and landing as expounded in (9), are formulated as a set of equality constraints $\mathbf{g}_1 \in \mathbb{R}^{28}$.

5.2.2 Conditions for feasible gaits

Maintaining a steady average moving speed v is accomplished by the constraint

$$g_2 := v - \frac{\ell_{\text{step}}}{t_{\text{step}}} = 0. \tag{19}$$

In addition, the guard functions of the transition surfaces defined in Sects. 3.4 and 3.5 are formulated as equality constraints:

$$g_3 := F_{1z}^- = 0, \qquad \text{(zero normal force before take-off)} \tag{20a}$$

$$g_4 := z_2^- = 0. \qquad \text{(front foot touches ground)} \tag{20b}$$

These are combined into a vector form of equality constraints $\mathbf{g} := [\mathbf{g}_1^\top, \ldots, g_4]^\top = \mathbf{0}$. A series of inequality constraints $\mathbf{h}(t_k) := [h_1, \ldots, h_{10}]^\top < \mathbf{0}$, which are evaluated at each discrete time step $t_k \in [0, t_{\text{step}}]$ of simulation, consist of the conditions in the SSP:

$$h_1 := -F_{1z}, \qquad h_2 := |F_{1,x}| - \mu_0 |F_{1,z}|, \tag{21a}$$

$$h_3 := z_1, \qquad h_4 := -z_2, \tag{21b}$$

$$h_5 := -\theta_{\text{K1}}, \qquad h_6 := -\theta_{\text{K2}}, \tag{21c}$$

and the FLP:

$$h_7 := -\theta_{\text{K1}}, \qquad h_8 := -\theta_{\text{K2}}, \tag{22a}$$

$$h_9 := -z_1, \qquad h_{10} := -z_2. \tag{22b}$$

Among these inequality constraints, (21a) enforces unilateral contacts of the stance foot without slipping;[5] (21b) requires that the stance foot (z_1) is not lift-off from the

[5] We assume the friction coefficient $\mu_0 = 0.6$ in the present study.

Table 1 Mechanical parameters of the five-link robot model

	upper body	thigh	shank
mass moment of inertia (in 10^{-3} kg m^2)	40.53	25.28	8.78
mass (in kg)	7.00	2.69	1.33
length (in m)	0.23	0.30	0.30
center of mass position (in m)	0.14	0.16	0.09

ground and the swing foot (z_2) does not scuff the ground; (21c) and (22a) forbid hyperextension of the knee joints; (22b) restricts that both feet do not touch the ground during the flight. These conditions form the vector of inequality constraints stated as $\mathbf{h} := [\mathbf{h}(0)^\top, \ldots, \mathbf{h}(t_k), \ldots, \mathbf{h}(t_{\text{step}})]^\top < \mathbf{0}$.

In addition, the optimization is restricted to finding stable limit cycles of the hybrid zero dynamics by the inequality constraint

$$h_\Lambda := |\Lambda| - 1 < 0, \tag{23}$$

where the largest magnitude $|\Lambda|$ of the Floquet multipliers, calculated from the projected monodromy matrix $\mathbf{D}_{\Sigma,\text{Run}}$ in (16), characterizes the stability of the periodic orbit, according to Sect. 4.3.2. The formulation presented in (24) is inspired by [60, 61], which seeks to identify stable, open-loop running gaits on rigid ground using a two-level optimization scheme. In their approach, energy-efficient gaits are optimized in the inner loop, while stability—characterized by the eigenvalues of the monodromy matrix—is handled in the outer loop. In contrast, our study employs a single-stage formulation, which significantly reduces evaluation time while still maintaining both efficiency and stability.

As a conclusion of the current section, we obtain the optimization problem

$$\begin{aligned} \min_{\boldsymbol{x}_{\text{opt}}} \quad & f(\boldsymbol{x}_{\text{opt}}) \\ \text{subject to} \quad & \mathbf{g} = \mathbf{0}, \\ & \mathbf{h} < \mathbf{0}, \\ & h_\Lambda < 0, \end{aligned} \tag{24}$$

which we solve with the SQP algorithm provided by the commercial software *Artelys Knitro*. Equations of motion are derived in the computer algebra system *Maple* and numerically evaluated using the programming language Julia. Derivatives are determined by the automatic differentiation algorithm from the Julia package *ForwardDiff.jl*.

6 Results and discussion

This study primarily contributes by designing a controller under the hybrid zero dynamics framework to analyze bipedal periodic running gaits on compliant surfaces. The main aim is to achieve high energy efficiency in generating a reference running gait that is periodic at a fixed average speed. This is accomplished by optimizing gait parameters in order to minimize the cost of transport. Stability and feasibility conditions of the simulated running are considered via inequality constraints in the optimization.

Optimization is performed for various average speeds within the set $v \in \{1.8, 1.9, \ldots, 3.3\}$ m/s. These outcomes are contrasted with studies on rigid ground running, extensively

explored in the literature, e.g. [51] and [53, Sect. 9]. Consequently, the modeling and controller design methodologies are employed from existing work without extensive elaboration in this manuscript. We employ the same optimization framework to reduce the bipedal running model to hybrid zero dynamics of lower dimensionality and determine periodic solutions using the multiple shooting method.

Parameters for the simulation robot model are sourced from a prototype under development, with dimensions of 0.83 m in height and a weight of 15.04 kg. Table 1 provides further mechanical details. The structure is as follows: Sect. 6.1 delves into the stability analysis of the optimized reference motion, and Sect. 6.2 examines energy efficiency alongside the reaction force and actuator torque when running on both rigid and compliant grounds.

6.1 Stability of reference gaits

As outlined in Sect. 4.3, the stability of the optimized reference gaits is evaluated using the largest magnitude $|\Lambda|$ of the nontrivial Floquet multipliers, which must be less than one. When this condition is satisfied, any initial deviations from the periodic solution decay asymptotically, ensuring that the gait stabilizes and converges to a steady periodic motion at the desired constant speed. Conversely, for unstable solutions, small deviations grow exponentially, causing the gait to diverge from the reference.

This section initiates the stability analysis with a study of running on rigid ground (see Sect. 6.1.1), a well-explored area in the literature. Subsequently, Sect. 6.1.2 provides a comparison of stability results on rigid versus compliant grounds. Closed-loop simulations offer insights into the limit cycles of the optimized reference running gait on both ground types.

6.1.1 Running on rigid ground

The framework for bipedal locomotion on rigid ground employs the identical robot model, consisting of five segments and a point foot, as that utilized for compliant ground. The principal difference arises in the representation of an inelastic impact at the point foot during the contact with rigid ground. In correspondence with the one degree of underactuation present during the single support phase, the limit cycle of the hybrid zero dynamics produces a (2×2)-dimensional monodromy matrix, which is derived analogously as delineated in (15). Among its two eigenvalues, one is trivial at unity owing to the system's autonomous nature, while the other nontrivial eigenvalue, known as the Floquet multiplier, signifies the rate of convergence to a stable limit cycle. More explicitly, a smaller multiplier denotes a more rapid convergence of perturbed solutions to the reference limit cycle. The orthogonal projection method, as detailed in (16), is utilized to directly compute the sole nontrivial eigenvalue, thus circumventing the QR iterations outlined in [59, Sect. 7.5].

In order to examine the relationship between energy efficiency and gait stability, a parameter study is conducted to illustrate the optimized cost of transport across various running speeds and Floquet multipliers, as depicted in Fig. 9. The findings indicate that, within the examined range of speeds, an enhancement in gait stability (achieved by reducing the magnitude of the largest Floquet multiplier) necessitates greater energy expenditure.

6.1.2 Comparison between rigid and compliant grounds

Figure 10 illustrates the magnitude of the largest Floquet multiplier $|\Lambda|$ for locomotion on both compliant and rigid grounds. Importantly, the multipliers remain marginally below

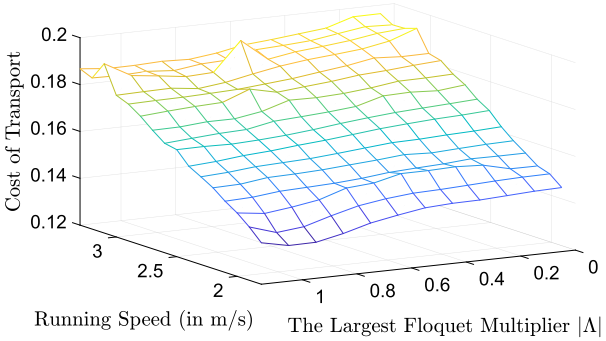

Fig. 9 Optimized cost of transport of running on rigid ground for the given target speeds and magnitudes of the largest Floquet multiplier

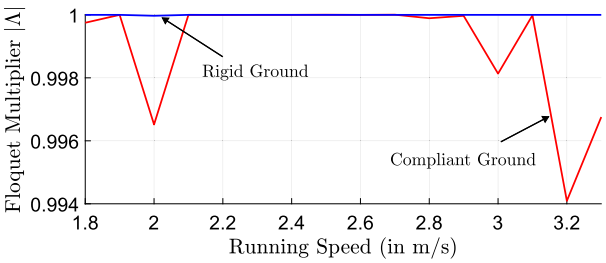

Fig. 10 Magnitude of the largest Floquet multiplier for the optimal walking and running gaits on compliant and rigid grounds

unity under all conditions examined, implying the stability of the solutions. Regarding running on rigid ground, depicted in Fig. 9, a decrease in the multiplier $|\Lambda|$ is associated with diminished energy efficiency, consequently leading to an increased cost of transport. Therefore, in efforts to minimize energy consumption while maintaining the largest multiplier $|\Lambda|$ beneath one, it is likely that the resultant multiplier will be proximate to, yet slightly below, unity.

The stability of running on compliant ground is not easily modified through adjustments in gait parameters. Establishing an optimization objective $\tilde{f}(\boldsymbol{x}_{\text{opt}}) = |\Lambda|$ to directly minimize the Floquet multiplier's magnitude $|\Lambda|$ does not yield smaller multipliers than shown in Fig. 10. Similarly, minimizing the largest singular value of the saltation matrices for discontinuous mappings, as suggested in [62], is ineffective in reducing the Floquet multiplier. We believe that running stability on compliant ground is attributed to three-dimensional underactuation in both single support and flight phases. Specifically, the relevant coordinates, particularly velocity components, undergo continuous transitions between phases. For instance, the angular momentum with respect to the robot's center of mass is used as an independent coordinate in both underactuated SSP and FLP, which remains constant during take-off (Sect. 3.4) and landing transitions (Sect. 3.5). This constancy also applies to linear momentum based on velocity coordinates. Thus, small perturbations to the system states persist near the periodic orbit, as indicated by a Floquet multiplier $|\Lambda| \approx 1$.

Conversely, locomotion on rigid ground results in a significant alteration. For example, the translational velocity of the contacting foot, previously the swing foot during the preceding flight phase, becomes zero due to the inelastic impact. Additionally, the angular momentum assessed around the center of mass experiences a discontinuity in accordance with the impact mapping on rigid ground, as elucidated in [53, Equation (3.110)]. Consequently, perturbations in state may be attenuated via discrete reset mappings, culminating in a stable periodic solution, as illustrated in Fig. 9.

We suggest that a gradual transition should occur when moving from running on compliant ground surfaces to rigid ones as the ground's stiffness and damping parameters in equation (1a)–(1b) progressively increase. This adjustment results in significant impulsive alterations in velocity coordinates and diminished motion of the stance foot, thereby emulating the dynamics observed on rigid ground. Nevertheless, our current optimization approach encounters considerable difficulty in obtaining periodic solutions that adhere to constraints when stiffness is increased, complicating the numerical solution of the SSP equations. Consequently, this manuscript does not include ground parameter variations. To further investigate stability, we suggest exploring alternative numerical techniques for addressing the significant underactuation in hybrid zero dynamics control, complicated by contact dynamics governed by stiff differential equations. For example, [45] employs the direct collocation method to facilitate gait generation for bipedal walking with many degrees of freedom, but it is unclear if this method can reliably approximate the contact dynamics in running gaits.

Running gaits with slippage can also be examined through our framework. Reference [53, p. 278] considers compliant ground as a model perturbation to test the stability of gaits initially designed for rigid ground. Their forward time simulation results indicate that while the limit cycle changes with respect to the reference on rigid ground, a stable limit cycle forms, implying stability in slipping scenarios on compliant surfaces. However, they do not offer a systematic stability analysis, and their stiffness parameter is about 440 times higher than in our work. Thus, additional research is needed to ascertain if stability is due to the slipping stance foot in the single support phase or the increased ground stiffness.

6.1.3 Closed-loop simulation

To assess the stability of the optimized running gaits, closed-loop simulations are performed using high-gain PD feedback[6] as described in Sect. 4. The simulations of the running gaits are conducted at a speed of 2.0 m/s on both rigid and compliant grounds, considering 20% initial discrepancies in the velocity coordinates of the four actuated joints relative to the reference. The initial velocity error is highlighted, given that, in practical experiments, adjusting the velocity of the robot's joints poses a greater challenge than configuring the precise joint angles prescribed by the reference gait. For improved visualization and validation of the convergence characteristics of the perturbed periodic solution, the reference gaits are established by imposing the magnitude of the Floquet multiplier $|\Lambda| < 0.9$. As depicted in Fig. 10, utilizing outcomes with Floquet multipliers slightly less than one leads to a situation where the initial deviations are nearly preserved.

Figure 11 particularly demonstrates the progression of actuated joint velocities with respect to the corresponding joint angles across ten sequential steps. Following each step, the exchange between the leading and trailing legs takes place, with each step's simulation employing the state variables derived from the previous one as initial conditions. Consequently, the trajectories shown in Fig. 11 are indicative of a closed loop. The simulation effectively validates that the closed-loop system maintains its limit cycle on both rigid and compliant grounds, despite minor initial perturbations. Notably, on rigid ground, Fig. 11 (Left) reveals discontinuities in the system states due to inelastic impacts and take-off events. Conversely, Fig. 11 (Right) illustrates relatively smooth state transitions during the discrete landing and take-off events.

Simulation results indicate that the generated running gait is highly sensitive to the chosen ground parameters within the compliant ground model. The closed-loop simulation applies a high-gain feedback law to ensure the system follows the zero dynamics manifold

[6] Feedback gains $\mathbf{K_P} = 1000$, $\mathbf{K_D} = 1000$ are used in the simulation.

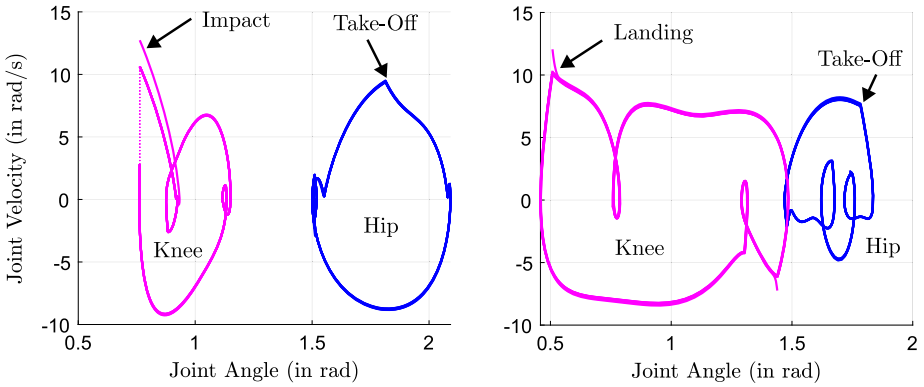

Fig. 11 Depiction of the running simulation as presented in 2.0 m/s, showcasing the behavior on rigid (Left) and compliant ground (Right). The presence of a dotted line signifies the discrete transition phase

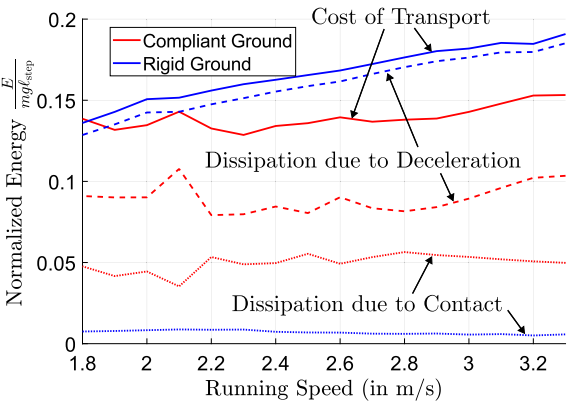

Fig. 12 The Cost of Transport (CoT) and normalized energy dissipation attributed to contact on rigid and compliant grounds, as well as deceleration employing electric motors

outlined in (12a)–(12b). Due to the large stiffness parameter used in this study, even slight control deviations cause notable alterations in the ground reaction force, significantly impacting system dynamics and the resulting gait.

6.2 Efficiency study

Figure 12 presents the optimized cost of transport and energy dissipation across various speeds for both ground models. In particular, the energy consumption and the energy dissipation are normalized against step length and robot weight, mirroring the cost of transport equation (17), to standardize energy assessments for comparison.

On rigid ground, efficiency is nearly linearly related to speed. In contrast, on compliant ground, efficiency remains roughly constant for speeds $v < 2.9\,\text{m/s}$. The overall energy efficiency of running on compliant surfaces is enhanced within the examined range of speeds, owing to the robot's ability to exploit the ground elasticity. This elasticity facilitates the temporary storage and subsequent recovery of kinetic energy as elastic energy during both compression and restitution phases, thereby reducing the amount of work required from the actuator.

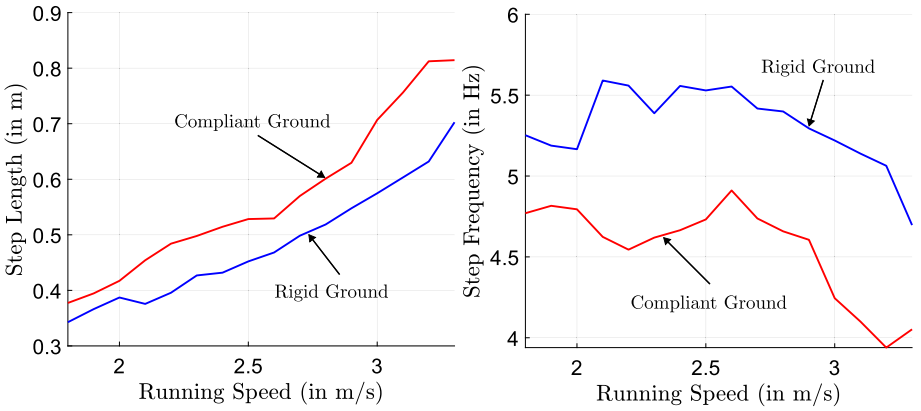

Fig. 13 Step length (Left) and step frequency (Right) of optimized running gaits on rigid and compliant grounds

Figure 13 depicts the analysis of optimal gaits concerning step length and frequency. Primarily, variations in running speed are due to changes in step length, with step frequency showing minimal variation. Compared to rigid surfaces, running on compliant ground in Fig. 13 (Right) results in lower step frequency due to ground deformation. As rigid ground can be regarded as a model with infinite stiffness, increasing the stiffness parameter in the compliant ground model could enhance the optimal step frequency, falling between the two scenarios shown.

6.2.1 Energy losses

Another perspective on the efficiency analysis involves examining the energy dissipation caused by contact with both rigid and compliant grounds, shown in Fig. 12 (dotted lines), and the energy loss during movement deceleration via electric motors, depicted in Fig. 12 (dashed lines). With periodic running regarded as limit cycles, the total energy remains unchanged, balancing total input (cost of transport) and losses due to ground contact and actuator deceleration. Electric energy regenerates as actuators decelerate, which is excluded from the cost of transport in equation (17).

As illustrated in Fig. 12 (dotted lines), the energy dissipation resulting from impacts on rigid ground is notably lower than that arising from damping on compliant ground, as detailed in Sect. 3.1. When contrasted with the actuator's deceleration-related energy losses depicted in Fig. 12 (dashed lines), the energy losses attributed to ground interactions are relatively minor. The deceleration-induced energy losses on rigid ground demonstrate a linear correlation with speed. Conversely, the presence of compliant ground facilitates the deceleration of the robot's movement, thereby markedly diminishing the actuator's deceleration energy losses and ultimately enhancing the overall energy efficiency of locomotion.

6.2.2 Reaction force on ground

Figure 14 depicts the reaction forces on the stance foot in both tangential and normal directions during running at 2.0 m/s on compliant and rigid grounds. With static friction ensuring no-slip contact, these forces are confined to the friction cone, as defined by constraint (21a). The unilateral contact condition ensures the normal forces are positive.

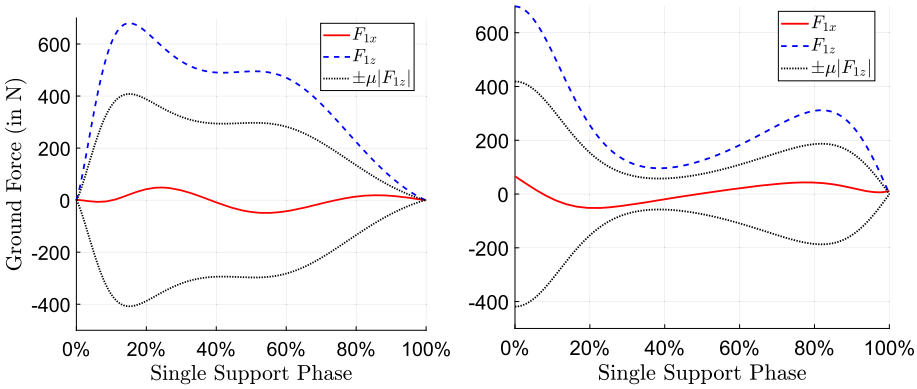

(a) Running on compliant ground. (b) Running on rigid ground.

Fig. 14 Reaction forces $\mathbf{F}_1 := [F_{1x}, F_{1z}]^\top$ on compliant (a) and rigid (b) grounds during the SSP of running at 2.0 m/s. Dotted lines show the maximum horizontal force without slippage, per $\mu = 0.6$

On rigid ground, tangential and normal forces reach their peak immediately following inelastic impact. By the conclusion of the SSP, the normal force diminishes to zero, and the robot initiates the flight phase. On compliant ground, both tangential and normal forces gradually increase from zero at SSP onset. Notably, the tangential force on compliant surfaces displays significant oscillations, essential for meeting feasibility conditions during running. As illustrated in Fig. 14a, the stance foot on compliant ground exhibits reduced slippage potential, whereas Fig. 14b indicates a higher likelihood of slipping on rigid ground during the middle of the SSP. This potential for slippage increases significantly with higher running speeds. Furthermore, the vertical normal forces have nearly equal maximum magnitudes, suggesting a minor influence of ground compliance on peak normal force.

6.2.3 Actuator

At an equivalent running speed 2.0 m/s on both rigid and compliant grounds, the actuator torques during the SSP and FLP are illustrated in Fig. 15. Similar to the ground response force, actuators, particularly those in the hip joints, display an impulsive escalation subsequent to the inelastic impact on rigid ground, posing a potential risk of damage to the drive train. During the mid and latter portions of the SSP, the actuators typically generate substantially reduced torque, as the robot leverages its passive dynamics to advance forward, optimizing energy expenditure.

In contrast, on compliant surfaces, the actuators escalate from a baseline of zero without abrupt jumps. Nevertheless, throughout the entirety of the SSP, continuous actuation is imperative to fulfill contact conditions, which are notably more intricate on compliant ground.

The compliant nature of the ground results in a significant reduction in actuator torque needed for movement, allowing for the use of smaller actuators with minimal impact from actuator saturation. Moreover, the smooth variations in the reference torque signal simplify the controller's responsiveness compared to the complex real-time adjustments required for abrupt changes on rigid surfaces.

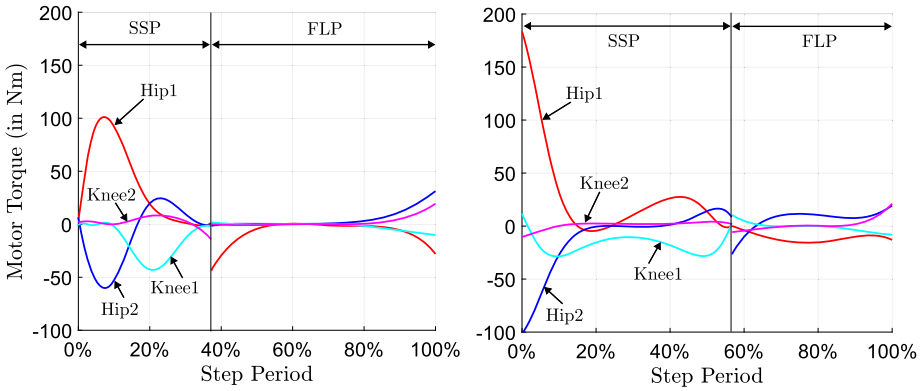

Fig. 15 Actuator torques required for running at 2.0, m/s on rigid (Right) and compliant ground (Left). The stance leg is denoted as 1, and the swing leg as 2

7 Conclusions

This study presents a control design within the framework of hybrid zero dynamics to enable stable and energy-efficient running gaits for a bipedal robot on compliant ground, expanding on previous work focused on rigid ground. The robot model consists of five rigid segments connected by four actuated revolute joints, ending with point feet. Its periodic running gait, maintaining a constant average speed determined by step length and duration, includes two continuous phases (single support and flight) and two discrete transitions (take-off and landing), forming a hybrid dynamical system. Non-slipping contact during the single support phase is modeled using nonlinear viscoelastic contact models.

Virtual constraints are utilized to represent the robot's running gait through reduced-order hybrid invariant zero dynamics, with periodic solutions identified via a multiple shooting method. The development of energy-efficient running gaits is formulated as an optimization problem focused on the reference trajectory, incorporating constraints for gait stability and physical feasibility. Orbital stability is evaluated using Floquet theory, and optimization is executed using a sequential quadratic programming algorithm.

Ground compliance introduces significant challenges, notably expanding the invariant zero dynamics manifold from two to six dimensions compared to rigid ground, and increasing sensitivity in the differential equations during contact. These challenges are addressed through a proposed multiple shooting formulation and an orthogonal projection of the monodromy matrix to isolate critical nontrivial Floquet multipliers. Using these methodologies, stable and efficient running gaits are achieved on compliant ground. A comparative study reveals that while energy dissipation from damping is greater on compliant ground surfaces compared to inelastic impacts on rigid surfaces, such compliance can still be used to attain energy-efficient running gaits. An added advantage of compliant ground is the absence of impulsive jumps in ground reaction forces and actuator torques upon landing, reducing potential mechanical damage to components like drive trains. The proposed framework can also be applied to the design of sports floors and surfaces. The software suite for simulating and optimizing running gaits on compliant ground is detailed in [63].

Future work will focus on refining numerical methods or exploring alternative approaches to address the high-dimensional, nonlinear, and stiff differential equations that arise during contact, facilitating the simulation of stiffer ground materials. This is expected

to provide deeper insights into smooth transitions between running gaits as ground properties shift from compliant to rigid. This study presumes decoupled normal and tangential contact force models and a constant friction coefficient. Future research could investigate the effects of coupling these forces and varying the friction coefficient according to contact conditions. Additionally, plans include incorporating sticking-slipping motion into the contact model, requiring advanced numerical techniques to handle increased discontinuities and uncertain sequences of continuous dynamics.

Acknowledgements The AI tool Writefull is employed to refine text formulation and correct grammatical inaccuracies.

Author contributions Yinnan Luo wrote the main manuscript and, together with Philipp Arbogast, implemented the simulations. Ulrich J. Römer and Alexander Fidlin provided methodological suggestions related to the study. All authors reviewed and improved the manuscript.

Funding information Open Access funding enabled and organized by Projekt DEAL.

Data availability No datasets were generated or analysed during the current study.

Declarations

Competing interests The authors declare no competing interests.

References

1. Kolvenbach, H., Bärtschi, C., Wellhausen, L., Grandia, R., Hutter, M.: Haptic inspection of planetary soils with legged robots. IEEE Robot. Autom. Lett. **4**(2), 1626–1632 (2019). https://doi.org/10.1109/LRA.2019.2896732
2. Fahmi, S., Focchi, M., Radulescu, A., Fink, G., Barasuol, V., Semini, C.: STANCE: locomotion adaptation over soft terrain. IEEE Trans. Robot. **36**(2), 443–457 (2020). https://doi.org/10.1109/TRO.2019.2954670
3. Collins, S., Ruina, A., Tedrake, R., Wisse, M.: Efficient bipedal robots based on passive-dynamic walkers. Science **307**(5712), 1082–1085 (2005). https://doi.org/10.1126/science.1107799
4. Reher, J., Ames, A.: Dynamic walking: toward agile and efficient bipedal robots. Annu. Rev. Control Robot. Auton. Syst. **4**, 535–572 (2021). https://doi.org/10.1146/annurev-control-071020-045021
5. Flores, P.: Contact mechanics for dynamical systems: a comprehensive review. Multibody Syst. Dyn. **54**(2), 127–177 (2022). https://doi.org/10.1007/s11044-021-09803-y
6. Sugihara, T., Morisawa, M.: A survey: dynamics of humanoid robots. Adv. Robot. **34**(21–22), 1338–1352 (2020). https://doi.org/10.1080/01691864.2020.1778524
7. Dubois, F., Acary, V., Jean, M.: The contact dynamics method: a nonsmooth story. C. R., Méc. **346**(3), 247–262 (2018). https://doi.org/10.1016/j.crme.2017.12.009
8. Pfeiffer, F.: On non-smooth multibody dynamics. Proc. Inst. Mech. Eng. Part K, J. Multi-Body Dyn. **226**(2), 147–177 (2012). https://doi.org/10.1177/1464419312438487
9. Ma, W.-L., Or, Y., Ames, A.D.: Dynamic walking on slippery surfaces: demonstrating stable bipedal gaits with planned ground slippage. In: 2019 International Conference on Robotics and Automation (ICRA), pp. 3705–3711 (2019). https://doi.org/10.1109/ICRA.2019.8793761

10. Sreenath, K., Park, H.-W., Poulakakis, I., Grizzle, J.: Embedding active force control within the compliant hybrid zero dynamics to achieve stable, fast running on MABEL. Int. J. Robot. Res. **32**(3), 324–345 (2013). https://doi.org/10.1177/0278364912473344
11. Reher, J., Ma, W.-L., Ames, A.D.: Dynamic walking with compliance on a cassie bipedal robot. In: 2019 18th European Control Conference (ECC), pp. 2589–2595 (2019). https://doi.org/10.23919/ECC.2019.8796090
12. Reher, J.P., Hereid, A., Kolathaya, S., Hubicki, C.M., Ames, A.D.: Algorithmic foundations of realizing multi-contact locomotion on the humanoid robot DURUS. In: Springer Proceedings in Advanced Robotics, pp. 400–415. Springer, Cham (2020). https://doi.org/10.1007/978-3-030-43089-4_26
13. Hubicki, C., Grimes, J., Jones, M., Renjewski, D., Spröwitz, A., Abate, A., Hurst, J.: ATRIAS: design and validation of a tether-free 3D-capable spring-mass bipedal robot. Int. J. Robot. Res. **35**(12), 1497–1521 (2016). https://doi.org/10.1177/0278364916648388
14. Gan, Z., Yesilevskiy, Y., Zaytsev, P., Remy, C.D.: All common bipedal gaits emerge from a single passive model. J. R. Soc. Interface **15**(146), 20180455 (2018). https://doi.org/10.1098/rsif.2018.0455
15. Flores, P.: A parametric study on the dynamic response of planar multibody systems with multiple clearance joints. Nonlinear Dyn. **61**(4), 633–653 (2010). https://doi.org/10.1007/s11071-010-9676-8
16. Flores, P., Ambrósio, J., Lankarani, H.M.: Contact-impact events with friction in multibody dynamics: back to basics. Mech. Mach. Theory **184**, 105305 (2023). https://doi.org/10.1016/j.mechmachtheory.2023.105305
17. Hertz, H.: Ueber die Berührung fester elastischer Körper. J. Reine Angew. Math. **1882**(92), 156–171 (1882). https://doi.org/10.1515/crll.1882.92.156
18. Seifried, R., Schiehlen, W., Eberhard, P.: The role of the coefficient of restitution on impact problems in multi-body dynamics. Proc. Inst. Mech. Eng. Part K, J. Multi-Body Dyn. **224**(3), 279–306 (2010). https://doi.org/10.1243/14644193JMBD239
19. Flores, P., Machado, M., Silva, M.T., Martins, J.M.: On the continuous contact force models for soft materials in multibody dynamics. Multibody Syst. Dyn. **25**(3), 357–375 (2011). https://doi.org/10.1007/s11044-010-9237-4
20. Machado, M., Moreira, P., Flores, P., Lankarani, H.M.: Compliant contact force models in multibody dynamics: evolution of the Hertz contact theory. Mech. Mach. Theory **53**, 99–121 (2012). https://doi.org/10.1016/j.mechmachtheory.2012.02.010
21. Alves, J., Peixinho, N., Silva, M.T., Flores, P., Lankarani, H.M.: A comparative study of the viscoelastic constitutive models for frictionless contact interfaces in solids. Mech. Mach. Theory **85**, 172–188 (2015). https://doi.org/10.1016/j.mechmachtheory.2014.11.020
22. Carvalho, A.S., Martins, J.M.: Exact restitution and generalizations for the Hunt–Crossley contact model. Mech. Mach. Theory **139**, 174–194 (2019). https://doi.org/10.1016/j.mechmachtheory.2019.03.028
23. Ghaednia, H., Wang, X., Saha, S., Xu, Y., Sharma, A., Jackson, R.L.: A review of elastic–plastic contact mechanics. Appl. Mech. Rev. **69**, 060804 (2017). https://doi.org/10.1115/1.4038187
24. Haug, E.: Simulation of friction and stiction in multibody dynamics model problems. Mech. Based Des. Struct. Mach. **46**(3), 296–317 (2018). https://doi.org/10.1080/15397734.2017.1341840
25. Ma, J., Chen, G., Ji, L., Qian, L., Dong, S.: A general methodology to establish the contact force model for complex contacting surfaces. Mech. Syst. Signal Process. **140**, 106678 (2020). https://doi.org/10.1016/j.ymssp.2020.106678
26. Liu, Q., Liang, J., Ma, O.: A physics-based and data-driven hybrid modeling method for accurately simulating complex contact phenomenon. Multibody Syst. Dyn. **50**(1), 97–117 (2020). https://doi.org/10.1007/s11044-020-09746-w
27. Yamamoto, K., Kamioka, T., Sugihara, T.: Survey on model-based biped motion control for humanoid robots. Adv. Robot. **34**(21–22), 1353–1369 (2020). https://doi.org/10.1080/01691864.2020.1837670
28. Tran Thien, H., Van Kien, C., Anh, H.P.H.: Optimized stable gait planning of biped robot using multi-objective evolutionary JAYA algorithm. Int. J. Adv. Robot. Syst. **17**(6), 1729881420976344 (2020). https://doi.org/10.1177/1729881420976344
29. Suleiman, W., Kanehiro, F., Miura, K., Yoshida, E.: Enhancing zero moment point-based control model: system identification approach. Adv. Robot. **25**(3–4), 427–446 (2011). https://doi.org/10.1163/016918610X551773
30. Meng, X., Yu, Z., Chen, X., Huang, Z., Dong, C., Meng, F.: Online running-gait generation for bipedal robots with smooth state switching and accurate speed tracking. Biomimetics **8**(1), 114 (2023). https://doi.org/10.3390/biomimetics8010114
31. Al-Shuka, H.F.N., Corves, B., Zhu, W.-H., Vanderborght, B.: Multi-level control of zero-moment point-based humanoid biped robots: a review. Robotica **34**(11), 2440–2466 (2016). https://doi.org/10.1017/S0263574715000107
32. Kuindersma, S., Deits, R., Fallon, M., Valenzuela, A., Dai, H., Permenter, F., Koolen, T., Marion, P., Tedrake, R.: Optimization-based locomotion planning, estimation, and control design for the atlas humanoid robot. Auton. Robots **40**(3), 429–455 (2016). https://doi.org/10.1007/s10514-015-9479-3

33. Hirukawa, H., Hattori, S., Harada, K., Kajita, S., Kaneko, K., Kanehiro, F., Fujiwara, K., Morisawa, M.: A universal stability criterion of the foot contact of legged robots - adios ZMP. In: Proceedings 2006 IEEE International Conference on Robotics and Automation, 2006. ICRA 2006, pp. 1976–1983 (2006). https://doi.org/10.1109/ROBOT.2006.1641995
34. Kashiri, N., Abate, A., Abram, S.J., Albu-Schaffer, A., Clary, P.J., Daley, M., Faraji, S., Furnemont, R., Garabini, M., Geyer, H., Grabowski, A.M., Hurst, J., Malzahn, J., Mathijssen, G., Remy, D., Roozing, W., Shahbazi, M., Simha, S.N., Song, J.-B., Smit-Anseeuw, N., Stramigioli, S., Vanderborght, B., Yesilevskiy, Y., Tsagarakis, N.: An overview on principles for energy efficient robot locomotion. Front. Robot. AI **5**, 129 (2018). https://doi.org/10.3389/frobt.2018.00129
35. Westervelt, E.R., Grizzle, J.W., Koditschek, D.E.: Hybrid zero dynamics of planar biped walkers. IEEE Trans. Autom. Control **48**(1), 42–56 (2003). https://doi.org/10.1109/TAC.2002.806653
36. Zhao, H., Nadubettu Yadukumar, S., Ames, A.D.: Bipedal robotic running with partial hybrid zero dynamics and human-inspired optimization. In: 2012 IEEE/RSJ International Conference on Intelligent Robots and Systems, pp. 1821–1827 (2012). https://doi.org/10.1109/IROS.2012.6386241
37. Grizzle, J.W., Chevallereau, C., Sinnet, R.W., Ames, A.D.: Models, feedback control, and open problems of 3D bipedal robotic walking. Automatica **50**(8), 1955–1988 (2014). https://doi.org/10.1016/j.automatica.2014.04.021
38. Guzelbulut, C., Shimono, S., Suzuki, K.: Optimization of human gait using singular-value decomposition-based design variables. Multibody Syst. Dyn. **59**(3), 255–267 (2023). https://doi.org/10.1007/s11044-023-09885-w
39. Pratt, J., Chew, C.-M., Torres, A., Dilworth, P., Pratt, G.: Virtual model control: an intuitive approach for bipedal locomotion. Int. J. Robot. Res. **20**(2), 129–143 (2001). https://doi.org/10.1177/02783640122067309
40. Plestan, F., Grizzle, J.W., Westervelt, E.R., Abba, G.: Stable walking of a 7-DOF biped robot. IEEE Trans. Robot. Autom. **19**(4), 653–668 (2003). https://doi.org/10.1109/TRA.2003.814514
41. Williams, D.S., Martin, A.E.: Does a finite-time double support period increase walking stability for planar bipeds? J. Mech. Robot. **13**, 011019 (2020). https://doi.org/10.1115/1.4048832
42. Flores, P., Ambrósio, J.: On the contact detection for contact-impact analysis in multibody systems. Multibody Syst. Dyn. **24**(1), 103–122 (2010). https://doi.org/10.1007/s11044-010-9209-8
43. Hereid, A., Hubicki, C.M., Cousineau, E.A., Hurst, J.W., Ames, A.D.: Hybrid zero dynamics based multiple shooting optimization with applications to robotic walking. In: 2015 IEEE International Conference on Robotics and Automation (ICRA), pp. 5734–5740 (2015). https://doi.org/10.1109/ICRA.2015.7140002
44. Posa, M., Cantu, C., Tedrake, R.: A direct method for trajectory optimization of rigid bodies through contact. Int. J. Robot. Res. **33**(1), 69–81 (2014). https://doi.org/10.1177/0278364913506757
45. Hereid, A., Hubicki, C.M., Cousineau, E.A., Ames, A.D.: Dynamic humanoid locomotion: a scalable formulation for HZD gait optimization. IEEE Trans. Robot. **34**(2), 370–387 (2018). https://doi.org/10.1109/TRO.2017.2783371
46. Bordalba, R., Schoels, T., Ros, L., Porta, J.M., Diehl, M.: Direct collocation methods for trajectory optimization in constrained robotic systems. IEEE Trans. Robot. **39**(1), 183–202 (2023). https://doi.org/10.1109/TRO.2022.3193776
47. Hereid, A., Kolathaya, S., Ames, A.D.: Online optimal gait generation for bipedal walking robots using Legendre pseudospectral optimization. In: 2016 IEEE 55th Conference on Decision and Control (CDC), pp. 6173–6179 (2016). https://doi.org/10.1109/CDC.2016.7799218
48. Schwenzer, M., Ay, M., Bergs, T., Abel, D.: Review on model predictive control: an engineering perspective. Int. J. Adv. Manuf. Technol. **117**(5), 1327–1349 (2021). https://doi.org/10.1007/s00170-021-07682-3
49. Silva, M.F., Machado, J.A.T., Lopes, A.M.: Modelling and simulation of artificial locomotion systems. Robotica **23**(5), 595–606 (2005). https://doi.org/10.1017/S0263574704001195
50. Haug, E.J.: Simulation of spatial multibody systems with friction. Mechanics based design of structures and. Machines **46**(3), 347–375 (2018). https://doi.org/10.1080/15397734.2017.1377086
51. Chevallereau, C., Westervelt, E.R., Grizzle, J.W.: Asymptotically stable running for a five-link, four-actuator, planar bipedal robot. Int. J. Robot. Res. **24**(6), 431–464 (2005). https://doi.org/10.1177/0278364905054929
52. Luo, Y., Römer, U.J., Zirkel, M., Zentner, L., Fidlin, A.: Efficiency study of the non-instantaneous double support phase in HZD controlled bipedal robot. In: Lacarbonara, W. (ed.) Advances in Nonlinear Dynamics, vol. II, pp. 73–82. Springer, Cham (2024). https://doi.org/10.1007/978-3-031-50639-0_7
53. Westervelt, E.R., Grizzle, J.W., Chevallereau, C., Choi, J.-H., Morris, B.: Feedback Control of Dynamic Bipedal Robot Locomotion. CRC Press, Boca Raton (2018). https://doi.org/10.1201/9781420053739
54. Isidori, A.: Nonlinear Control Systems, 3rd edn. Springer, London (1995). https://doi.org/10.1007/978-1-84628-615-5

55. Müller, P.C.: Calculation of Lyapunov exponents for dynamic systems with discontinuities. Chaos Solitons Fractals **5**(9), 1671–1681 (1995). https://doi.org/10.1016/0960-0779(94)00170-U
56. Adolfsson, J., Dankowicz, H., Nordmark, A.: 3D passive walkers: finding periodic gaits in the presence of discontinuities. Nonlinear Dyn. **24**(2), 205–229 (2001). https://doi.org/10.1023/A:1008300821973
57. Nayfeh, A.H., Balachandran, B.: Applied Nonlinear Dynamics: Analytical, Computational, and Experimental Methods. Wiley, Hoboken (1995). https://doi.org/10.1002/9783527617548. First published: 29 March 1995, Online ISBN: 978-3-527-61754-8
58. Kong, N.J., Joe Payne, J., Zhu, J., Johnson, A.M.: Saltation matrices: the essential tool for linearizing hybrid dynamical systems. Proc. IEEE **112**(6), 585–608 (2024). https://doi.org/10.1109/JPROC.2024.3440211
59. Golub, G.H., Van Loan, C.F.: Matrix Computations, 4th edn. Johns Hopkins University Press, Baltimore (2013)
60. Mombaur, K.D., Longman, R.W., Bock, H.G., Schlöder, J.P.: Open-loop stable running. Robotica **23**(1), 21–33 (2005). https://doi.org/10.1017/S026357470400058X
61. Mombaur, K.D., Bock, H.G., Schlöder, J.P., Longman, R.W.: Open-loop stable solutions of periodic optimal control problems in robotics. Z. Angew. Math. Mech. **85**(7), 499–515 (2005). https://doi.org/10.1002/zamm.200310190
62. Tucker, M., Csomay-Shanklin, N., Ames, A.D.: Robust bipedal locomotion: leveraging saltation matrices for gait optimization. In: 2023 IEEE International Conference on Robotics and Automation (ICRA), pp. 12218–12225 (2023). https://doi.org/10.1109/ICRA48891.2023.10161309
63. Luo, Y.: julia-software package for bipedal robot running on compliant ground using hybrid zero dynamics controller. KITopen (2025). https://doi.org/10.35097/nvzaaubdprqr3vtm

Authors and Affiliations

Yinnan Luo[1] · Philipp Arbogast[1] · Ulrich J. Römer[2] · Marten Zirkel[3] · Lena Zentner[3] · Alexander Fidlin[1]

✉ Y. Luo
yinnan.luo@kit.edu

P. Arbogast
philipp.arbogast@kit.edu

U.J. Römer
Ulrich.Roemer@imfd.tu-freiberg.de

M. Zirkel
marten.zirkel@tu-ilmenau.de

L. Zentner
lena.zentner@tu-ilmenau.de

A. Fidlin
alexander.fidlin@kit.edu

1 Institute of Engineering Mechanics, Karlsruhe Institute of Technology, Kaiserstraße 10, Karlsruhe, 76131, Germany

2 Institute of Mechanics and Fluid Dynamics, TU Bergakademie Freiberg, Lampadius-Str. 4, Freiberg, 09599, Germany

3 Compliant Systems Group, Ilmenau University of Technology, Max-Planck-Ring 12, Ilmenau, 98684, Germany